# Spatially and temporally dense measurements reveal meteorological driver of atmospheric mercury variability

*Eric M. Roy[1,2]*, David A. Gay[3], Noelle E. Selin[1,2,4]*

[1]Department of Earth, Atmospheric, and Planetary Sciences, Massachusetts Institute of Technology, Cambridge, MA, USA

[2]Center for Sustainability Science and Strategy, Massachusetts Institute of Technology, Cambridge, MA, USA

[3]National Atmospheric Deposition Program, Wisconsin State Laboratory of Hygiene, University of Wisconsin Madison, Madison, WI, USA

[4]Institute for Data, Systems, and Society, Massachusetts Institute of Technology, Cambridge, MA, USA

KEYWORDS: Mercury, Gaseous Elemental Mercury, Chemical Transport Modeling, Box modeling, Diel variability, Atmospheric rectifier effect

ABSTRACT: The environmental fate of mercury (Hg) is determined by its atmospheric processing, yet the relative role of surface fluxes, chemistry, and transport on atmospheric loadings remains poorly understood. We use multiyear gaseous elemental Hg ($Hg^0$) concentration measurements at two rural sites and two urban sites in the northeastern US coordinated by the National Atmospheric Deposition Program (NADP) together with models to identify drivers of diel variability. We observe that $Hg^0$ concentrations have similar magnitude and variability between measurement sites within urban or rural regions, with highest concentrations in the urban region. Concentrations within the rural and urban regions tend to converge at midday, reaching a maximum at rural sites and a minimum at urban sites, particularly in summer. Using a boundary layer box model and the GEOS-Chem chemical transport model, we show that this midday convergence is driven by the combined influence of regional surface fluxes and the entrainment of free tropospheric air, rather than in-situ chemical fluxes. Our results demonstrate that diel $Hg^0$ concentration variability can serve as a constraint on free tropospheric loadings of $Hg^0$ and can help identify biases in regional and global atmospheric budgets of Hg.

## 1 Introduction

Mercury (Hg) is a globally distributed neurotoxic pollutant which is subject to complex atmospheric processing that determines its deposition to vulnerable ecosystems[1–3]. Historical and ongoing anthropogenic activities have introduced significant quantities of Hg to the environment over the last four millennia, leading to an eightfold increase in its atmospheric burden[4,5]. The rate at which Hg is removed from the atmosphere is largely determined by its chemical speciation, which includes gaseous elemental Hg ($Hg^0$, >90% of tropospheric burden) along with gaseous and particulate-bound oxidized Hg ($Hg^{II}$, <10% of tropospheric burden)[6–8]. $Hg^0$ has a long atmospheric lifetime and is removed by vegetative uptake or oxidation to $Hg^{II}$ [8,9], while $Hg^{II}$ is highly soluble and readily removed from the atmosphere via wet or dry deposition[10,11], or may be converted to

$Hg^0$ via photoreduction[8,12]. In addition to direct anthropogenic and geogenic Hg emissions, previously deposited mercury can be reemitted from surfaces, leading to its continual recycling in the environment[5]. Therefore, the atmospheric concentration of Hg at a given location will be determined by the combined influence of emission, deposition, chemistry, and atmospheric transport processes that act on local to global scales.

Global growth in the number of atmospheric Hg monitoring sites over the last three decades has helped researchers investigate its spatial and temporal variability, though mechanisms remain contested. Long term $Hg^0$ measurements made possible by national and international monitoring networks have shown that average Hg concentrations in urban regions are often higher than rural regions, consistent with the expected impact of anthropogenic emissions[13,14]. These observations have also shown that diel variations of atmospheric $Hg^0$ in urban and rural regions are effectively out of phase with one another, with $Hg^0$ lowest at midday at urban sites and highest at midday at rural sites. Early studies observed that this daytime decline of $Hg^0$ at urban sites coincided with a daytime maximum in $Hg^{II}$ and argued that this variability could be explained by $O_3$-mediated oxidation in polluted regions[15,16]. However, a recent study using robust $Hg^{II}$ measurements found that these elevated $Hg^{II}$ concentrations were likely driven by free tropospheric input rather than in-situ oxidation[17]. In contrast to urban areas, $Hg^0$ concentrations in vegetated rural areas are typically highest at midday and lowest before dawn[18–20]. This pattern is counterintuitive given the growing consensus that vegetation acts as a net sink of $Hg^0$, where photosynthetically-driven uptake should be strongest at midday[21,22]. Studies have argued that daytime $Hg^0$ concentration peaks may be driven by the reemission of Hg from short-term reservoirs, including previously deposited $Hg^{II}$ on cuticular surfaces[23], or the uptake and subsequent reemission of Hg by dew formation and evaportation[23,24]. However, hypothesized reemission pathways were not observed in ecosystem-scale flux measurements carried out at two rural sites in the northeastern US, instead showing that underlying forests act as a strong sink during daylight hours and a slight sink overnight during vegetatively active seasons[25]. A recent controlled experiment found that tropical vegetation also acted as a strong sink during daylight hours and a weak sink overnight, though mechanisms for this variability remain unclear[26].

Previous studies have also argued that diel $Hg^0$ variability could be explained by boundary layer processing. Nair et al.[19] compared $Hg^0$ concentrations at urban, rural, and suburban sites in the southeastern US and used correlation-based arguments to conclude that boundary layer entrainment was a key driver of differences in diurnal variations across sites, rather than chemical fluxes. More recently, Roy et al.[20] compared the seasonal and diel variation of $Hg^0$ concentrations and $Hg^0$ ecosystem uptake fluxes at two rural forests in the northeastern US, finding that concentrations are highest when uptake fluxes are strongest, and argued that the out-of-phase behavior could be explained by the combined influence of variations in surface fluxes and the downwelling of free tropospheric air. Despite ample discussion in observational literature, the relative contribution of chemistry, surface fluxes, and transport fluxes (i.e., boundary layer entrainment, horizontal advection) to diel variability has not been extensively studied in existing chemical transport models (CTMs).

Here, we investigate the drivers of spatial and diel variation of $Hg^0$ concentrations at four measurement sites (two urban, two rural) in the northeastern US coordinated by the National Atmospheric Deposition Program (NADP) Atmospheric Mercury Network (AMNet). We first characterize the diel variation across the sites in both June and December, representing summer and winter months, respectively. We then use a boundary layer box model adapted from Denzler et al.[27] that is driven by observationally derived meteorology to calculate the regional surface fluxes that reproduce observed $Hg^0$ concentrations at rural and urban sites for a given set of boundary conditions. Finally, we compare the range of calculated regional surface fluxes to those used by the GEOS-Chem CTM and explore the relative sensitivity of modeled concentration variability to regional surface and transport fluxes.

## 2. Methods

We first describe the four measurement sites evaluated in this study (section 2.1), and then discuss the simple boundary layer box model that we use to investigate the drivers of concentration variability (section 2.2). Finally, we describe our implementation of the GEOS-Chem CTM and list the sensitivity simulations discussed in this paper (section 2.3).

### 2.1 Measurement Sites

Formally launched in 2009, NADP AMNet was designed to provide concentration measurements of $Hg^0$ and $Hg^{II}$ (gaseous and particulate-bound) that could be used, in part, to infer the dry deposition of Hg to North America[13]. We use $Hg^0$ measurements from four sites in the northeastern US that were active for at least one year between 2011 and 2019 (inclusive) and exclude analysis of $Hg^{II}$ based on its secondary contribution to atmospheric Hg burdens, along with the growing consensus that $Hg^{II}$ measurement techniques used by current networks exhibit a significant and spatially variable low bias[28]. We select the New Brunswick, NJ (NJ30) and The Bronx, NY (NY06) sites to represent urban conditions, located approximately 45 km SW and 15 km NE of midtown Manhattan, respectively. Measurements taken at the Huntington Wildlife Forest, NY (NY20) and on the slopes of Mt. Mansfield in Underhill, VT (VT99) are located approximately 400 km N of Manhattan and represent rural conditions (Figure 1). These sites were selected, as they exhibit seasonal and diel concentration variations that are consistent with previous regional analyses. While observations are also available for the Elizabeth, NJ site (NJ54) since

2015, we exclude this site from our analysis due to extremely high average concentrations, which suggest that this site is influenced by local pollution sources (Figure S1). One potential source is the Phillips 66 oil refinery that is located approximately 1 km WSW of NJ54, which is listed as the 7th largest Hg source in New Jersey by the 2020 EPA National Emission Inventory[29], among a number of other local sources that were identified by Aucott et al.[30].

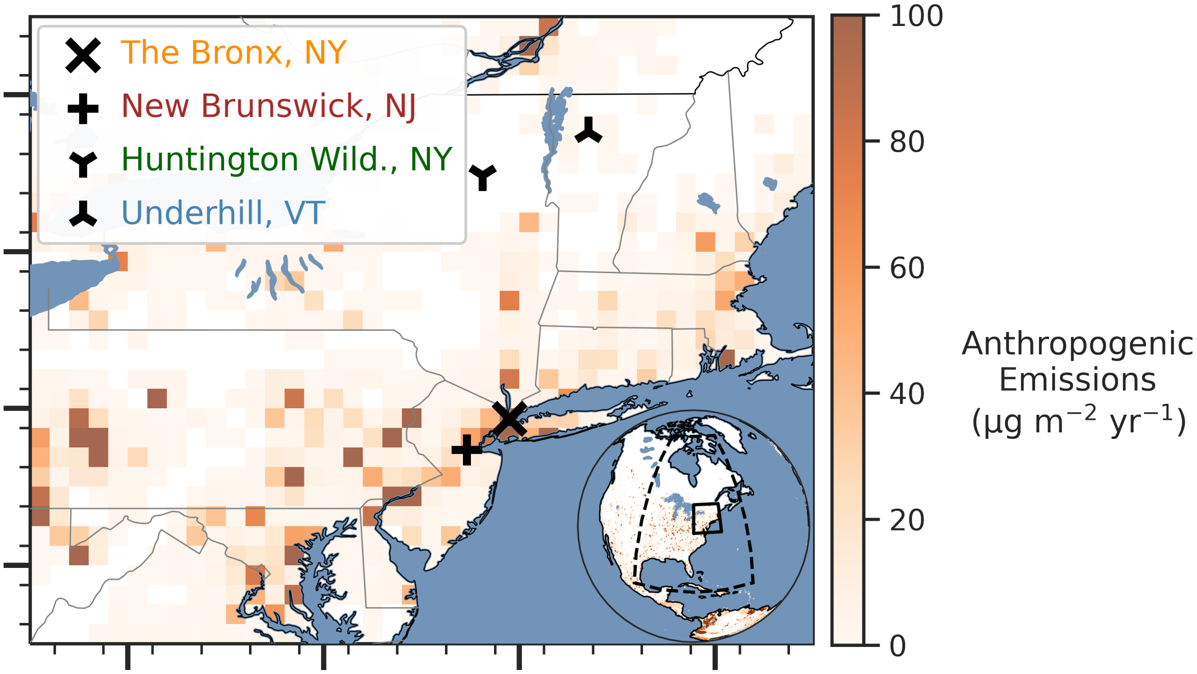

**Figure 1.** Location of rural (Underhill, VT and Huntington, NY) and urban (The Bronx, NY and New Brunswick, NJ) NADP sites explored in this study. Shading refers to the annual anthropogenic emissions predicted by the GMA emission inventory[31]. Major ticks represent the bounds of GEOS-Chem 2° latitude by 2.5° longitude grid boxes and minor ticks represent bounds of GEOS-Chem 0.5° latitude by 0.625° longitude grid boxes. Inset: The solid box represents the northeastern US domain, while the dashed box represents the entire domain covered by nested GEOS-Chem simulations.

## 2.2 Box model

We define a simple boundary layer box model following the approach of Denzler et al.[27] to model $Hg^0$ concentrations within the PBL ($c_{PBL}$) at rural and urban sites. The change in $Hg^0$ concentration within the PBL over time (ng m$^{-3}$ hr$^{-1}$) is defined by equation 1:

$$1. \qquad \frac{dc_{PBL}}{dt} = \frac{u(c_{UW} - c_{PBL}(t))}{x} + \frac{w_{PBL}(c_{FT} - c_{PBL}(t))}{z} + \frac{F}{z} + F_{chem}$$

where $u$ is the horizontal wind magnitude within the planetary boundary layer (PBL, m hr$^{-1}$), $w_{PBL}$ is the growth rate of the PBL (m hr$^{-1}$), $x$ is the horizontal extent of the box (m), $z$ is the vertical extent of the box (PBL height, or PBLH, with units m), $F$ is the surface flux within the box (ng m$^{-2}$ hr$^{-1}$), $F_{chem}$ is the net production of $Hg^0$ within the box (ng m$^{-3}$ hr$^{-1}$), and $c_{UW}$ and $c_{FT}$ represent the upwind and free tropospheric concentrations of $Hg^0$, respectively. From left to right, the four terms of equation 1 represent the horizontal advection flux, entrainment flux, the net surface exchange flux, and net chemical production. We neglect $F_{chem}$ in our box model and test this assumption in section 3.1 by comparing its magnitude in the GEOS-Chem CTM within the PBL to net surface fluxes.

We configure the box model to capture the average regional variability given an average set of meteorological conditions and fluxes, similar to the typical configuration of global CTMs. We first define $x$ to be 100 km, which is approximately equivalent to a 0.9° latitude by 0.9° longitude grid in this region. We then define $u$, $z$, and $w_{PBL}$ using a previously published dataset that provides hourly vertical profiles of horizontal windspeeds and PBLH calculated using aircraft data available at 50 airports within the continental US between 2010 and 2020[32,33]. We only use 2017 meteorological data due to interannual variations in the quantity and quality of aircraft-derived profiles. Regionally representative meteorological conditions are defined as the average of profiles collected at Newark Liberty International Airport (Newark, NJ) and Bradley International Airport (near Hartford CT). We then select the month of interest and calculate the average PBLH and horizontal windspeed for each respective hour, resulting in a single 24 hour diurnal cycle that is repeated for each day of the month. Due to the limited amount of data that are used to calculate these cycles ($n \leq 31$ data points for each hour), we apply a centered rolling average with a five hour window to define the average boundary layer variation for this region (Figure S2), which we find to be similar to the PBLH from the MERRA2 reanalysis product that drives GEOS-Chem (Figure S3). Using this smoothed profile, we calculate $w_{PBL}$ as the hourly change in PBLH. The entrainment term is nonzero only when $w_{PBL}$ is positive (i.e., dawn-midday)[27,34], as the communication of $C_{PBL}$ and $C_{FT}$ is mediated by convective thermals that overshoot the previous PBLH during periods of growth, while PBLH declines are caused by weakening convective thermals that do not reach the existing PBLH. We follow a similar approach to calculate a smooth, daily repeating pattern for $u$, which represents the average wind magnitude at each profile level that is below the PBLH (Figure S4).

We identify constant surface fluxes that minimize the difference between the boundary layer box model and the observed average $Hg^0$ concentration for the month and region of interest. We calibrate $F$ to minimize the residual between the box model average $Hg^0$ concentration and the observed monthly average $Hg^0$ concentration for a given combination of $c_{UW}$ and $c_{FT}$. This exercise is conducted for both June and December to isolate seasonal impacts. We use constant values of $F$ in our model based on previous studies that have shown that $Hg^0$ fluxes are generally unidirectional over day and night periods[20,25]. This is further justified in supplemental section S3, where we reevaluate this optimization while allowing fluxes to vary diurnally, which does not notably change the average surface flux and leads to overfitting of the model (Figures S5-S8).

### 2.3 GEOS-Chem

We simulate the atmospheric concentration of $Hg^0$ using the GEOS-Chem CTM (v14.1) to investigate its treatment of spatial and temporal variability at regional scales. This version of the model leverages the three-step oxidation mechanism described by Shah et al.[8] and the updated dry deposition scheme introduced by Feinberg et al.[6]. We drive the model with 2015 anthropogenic emissions produced for the 2018 Global Mercury Assessment[31] (Figure 1). Each simulation is run for 2018 and 2019, where 2018 data is discarded as model initialization. The model is run at its standard spatial resolution (2° latitude by 2.5° longitude with 47 vertical layers), which we refer to as the STND simulation. We then use this simulation to produce boundary conditions for a nested simulation (0.5° latitude by 0.625° longitude with 47 vertical layers) spanning eastern North America (20°-70° N, 50°-100° W, dashed box in Figure 1), allowing us to evaluate the impact of horizontal resolution on simulated $Hg^0$ concentrations, which we refer to as NEST.

We conduct eight sensitivity simulations based on the NEST simulation described above to evaluate the impact of enhancements to regional anthropogenic emission and free tropospheric loadings on surface concentrations at these sites (Table S1). We first assess the impact of anthropogenic emissions with three simulations where GMA emissions are scaled by factors of 3, 7 and 10 within the domain bounded by Figure 1 (70°W-80°W, 40°N-50°N), referred to as ANT3, ANT7, and ANT10, respectively. We specifically select enhancements of 3 and 7 based on the recommendations of an existing study of the Greater Boston area[35]. We run an additional three sensitivity simulations where emissions throughout the nested domain are scaled by 3, 7, and 10 to evaluate the impact of enhancing emissions across most of eastern North America, referred to as ANT3-ENA, ANT7-ENA, and ANT10-ENA, respectively. The two remaining sensitivity simulations use standard GMA anthropogenic emissions but uniformly increase free tropospheric $Hg^0$ concentrations throughout the nested domain to approximately 1.4 ng $m^{-3}$ (CFTSCAL) and 1.8 ng $m^{-3}$ (CFTSCALMAX), respectively, allowing us to assess the impact of free tropospheric loadings on surface concentrations.

## 3. Results and discussion

We first compare measured concentrations at the four sites to simulations of the GEOS-Chem model and our boundary layer box model, and discuss the possible contribution of chemistry, local surface fluxes, and transport fluxes to observed $Hg^0$ concentrations and their variability (section 3.1). We then conduct a sensitivity analysis to identify the relative contribution of regional surface fluxes and transport fluxes on biases in the GEOS-Chem model (section 3.2). After diagnosing the sensitivity of diel concentration variability to enhancements of regional surface fluxes and transport fluxes in the rural and urban regions (section 3.3), we discuss implications for Hg modeling and monitoring efforts (section 3.4).

### 3.1 Measured and modeled $Hg^0$ concentrations

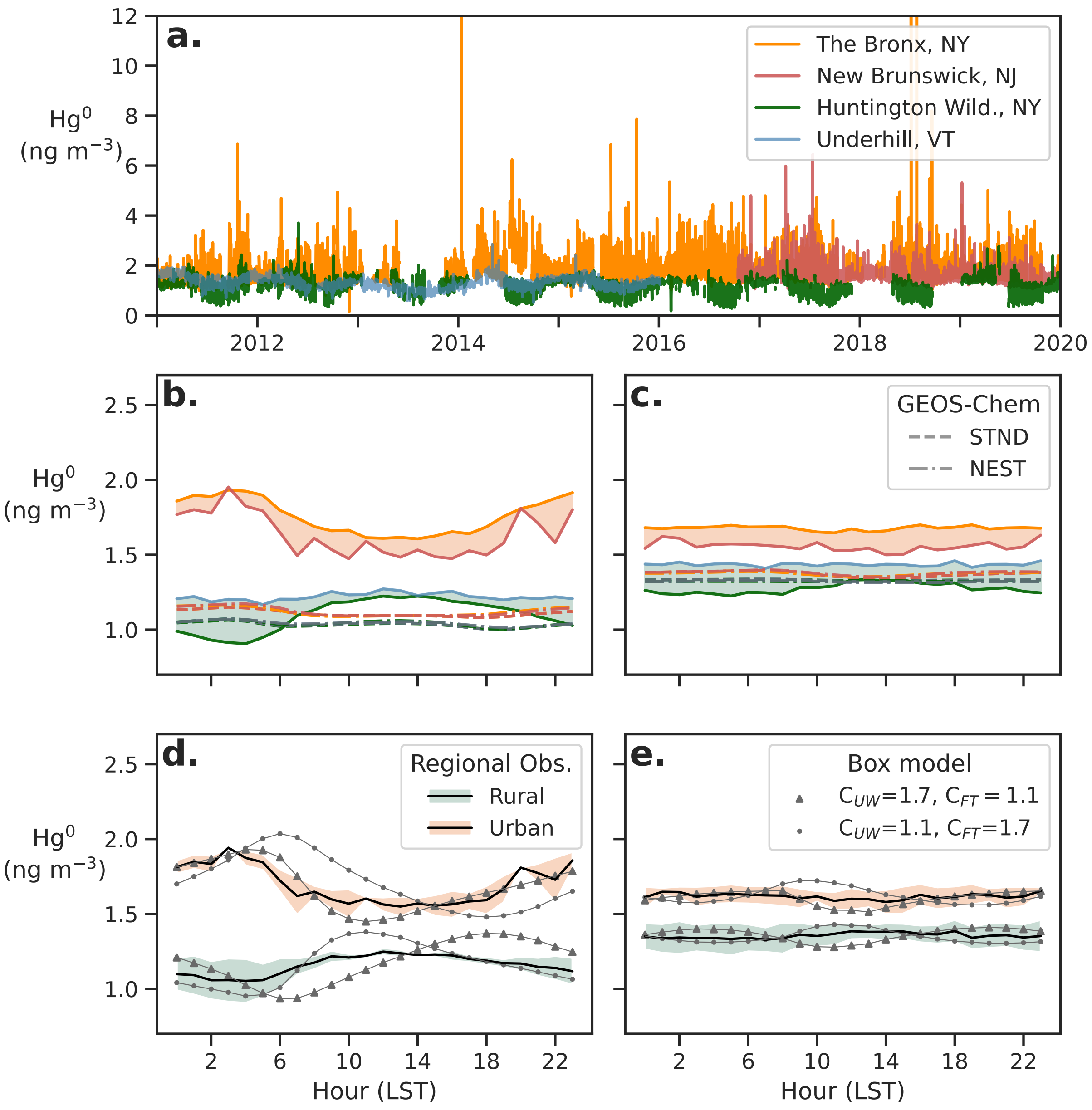

**Figure 2.** (a) Hourly concentrations at The Bronx (orange), New Brunswick NJ (red), Underhill VT (blue), and Huntington NY (green). (b) Average hourly concentrations for all four sites in June (solid lines, colors correspond with panel a), along with the diurnal cycles predicted by STND (dash) and NEST (dash-dot) simulations. Orange and green shading represent the range of observed concentrations at the urban and rural sites, respectively. (d) June diurnal cycles predicted by box model with $C_{UW}$=1.7 and $C_{FT}$=1.1 (triangle), and $C_{UW}$=1.1 and $C_{FT}$=1.7 (circle) are overlayed

on average urban and rural concentrations (black line) and their range (orange and green shading). Panels (c) and (e) are the same as (b) and (d), except for December.

The magnitude and variability of hourly $Hg^0$ concentrations are largely consistent within urban or rural regions but differ notably across region types at the four NADP sites considered (Figure 2a). Concentrations at urban sites are typically higher than rural sites, with the highest values observed at The Bronx and the lowest observed at Huntington. Concentrations at the rural sites exhibit expected northern hemispheric seasonality, where concentrations are highest in late winter and lowest in late summer, consistent with the previously identified vegetative control on $Hg^0$ concentrations[21–23]. Seasonality at urban sites is largely masked by strong summertime variability, with concentrations occasionally above 6 ng $m^{-3}$ at both urban sites and as high as 20 ng $m^{-3}$ at The Bronx, highlighting the occasional influence of local pollution sources. Concentrations at rural sites rarely exhibit discrete concentration peaks, but are most variable during summer months, when values consistently reach as low as 0.5 ng $m^{-3}$ at Huntington. Interestingly, urban concentrations throughout the measurement period appear to reach a lower bound that is nearly equivalent to the upper bound of concentrations at rural sites. This convergence point exhibits the same previously noted seasonality, except for one three-month period in early 2019 where concentrations at Huntington Wildlife exhibit unexpectedly high values.

Diel variations of $Hg^0$ concentrations at sites within a given region and month are similar, but variations at rural and urban sites are out-of-phase (Figures 2b, 2c). Concentrations at urban sites are highest at night and lowest at midday, while rural sites have the lowest concentrations before dawn and highest concentrations at midday. The consistency of concentration variations within regions provides confidence that these variations are regionally representative. A large concentration difference exists between urban and rural sites, with concentrations at rural sites 20-

45% lower than the values measured at urban sites for respective hours. We observe a notable convergence of $Hg^0$ concentrations at urban and rural sites at midday, similar to a previous multisite comparison in the southeastern US[19]. Spatial gradients persist in December, with concentrations remaining the lowest at Huntington and highest at The Bronx and rural concentrations 12-18% lower than urban values, however diel variation at all sites is negligible (Figure 2c). While concentrations at rural sites are between 10% (midday) and 21% (night) higher in December than in June, concentrations at the urban site are only 3% higher in December at midday and 20% lower on average during nocturnal hours. This seasonal difference largely reflects seasonal shifts in meteorological ventilation in the northeastern US, where stagnation and strong nocturnal inversions dominate during the summer and horizontal advection increases in the winter, thereby limiting the nocturnal buildup of concentrations (Figure S4). These differences in seasonality are also consistent with previous findings that seasonal variability may reflect the influence of regional surface fluxes and meteorology[20].

Both STND and NEST simulations fail to capture the strong spatial and diel variability observed at these four sites. In June, STND and NEST simulations underestimate observed concentrations at all four sites during the day, and underestimate concentrations at urban sites at all hours, exhibiting a negligible spatial gradient and minimal diel variation that is inconsistent with observed patterns (Figure 2b). In December, STND and NEST simulations exhibit a muted diel variation that is consistent with observations, however urban concentrations are underestimated at all hours (Figure 2c). The STND and NEST simulations also predict a seasonal variation in concentration magnitude that is generally consistent with average concentrations at rural sites. The nearly identical performance of STND and NEST simulations indicates that biases are not driven by the spatial smoothing induced by large grid cells.

We find that the contribution of chemical fluxes to diel variability in these regions is minor by comparing simulated net and gross chemical fluxes within the PBL to net surface fluxes for the NEST, ANT3, ANT7, and ANT10 simulations (Figure S9). These simulations estimate that net chemical fluxes of Hg within the PBL in June are 36-875 times smaller than net surface fluxes (normalized by average PBLH) at the rural sites and 21-30 times smaller at urban sites, underscoring the secondary role of chemical fluxes on the short-term $Hg^0$ concentration variability in this region. This is unsurprising given the long global lifetime $Hg^0$ against oxidation, which has ranged between 2.3-4.5 months in recent versions of GEOS-Chem[6–8].

The secondary contribution of in-situ chemical processing to diel variability is further supported by simulations of our boundary layer box model, which can capture the qualitative characteristics of diel variations in both urban and rural regions without considering fluxes from chemistry or short term reservoirs (Figures 2d and 2e). In June, we find that a constant surface flux of 12.6 ng $m^{-2}$ $hr^{-1}$ can best reproduce the observed monthly average urban concentration given $C_{UW}$=1.7 ng $m^{-3}$ and $C_{FT}$=1.1 ng $m^{-3}$, while a constant flux of -26.9 ng $m^{-2}$ $hr^{-1}$ best reproduces the observed average rural concentration. In December, we find that the box model bounded by the same values of $C_{UW}$ and $C_{FT}$ best reproduces observed monthly average urban concentration with a constant flux of -1.8 ng $m^{-2}$ $hr^{-1}$, while a flux of -30.5 ng $m^{-2}$ $hr^{-1}$ is required to reproduce the observed average rural concentration (Figure 2e). Although surface fluxes are only optimized to reproduce the monthly average regional concentration for the respective month, the boundary layer box model qualitatively reproduces dominant characteristics of diel variability at both sites in both months, with previously noted out-of-phase behavior in June and muted variations in December.

The diurnal convergence of $Hg^0$ concentrations across rural and urban regions in June highlights the important influence of boundary layer entrainment on surface concentration variability. Given that net chemical fluxes in the rural and urban regions considered are 2-3 orders of magnitude smaller than net surface fluxes, we confirm the diminished role of in-situ chemical fluxes on diel $Hg^0$ variability suggested by other studies[17,27]. The diurnal convergence of $Hg^0$ concentrations at urban and rural sites is most easily explained by atmospheric mixing, however this cannot be explained by horizontal advection given the distance between our regions (approximately 400 km). In the absence of horizontal mixing, $Hg^0$ concentrations aloft that have a smooth spatial variation would result in a similar midday convergence, as entrainment during morning PBL growth would dilute or enhance concentrations within the PBL depending on underlying surface fluxes. This is confirmed by our boundary layer box model, which qualitatively reproduces expected diel variations when forced by temporally invariant surface fluxes that are calibrated to reproduce monthly average concentrations. These results further suggest that similar adjustments to fluxes within the GEOS-Chem model could address biases in diel variations in STND and NEST simulations, without considering in-situ chemical fluxes or short-term reservoirs of Hg.

### 3.2. Solution spaces of optimized fluxes in urban and rural regions

To account for the unknown magnitude of $C_{FT}$ and $C_{UW}$, we repeat the box model optimization across a conservative range of $C_{FT}$ and $C_{UW}$ estimates (1-2 ng $m^{-3}$) for rural (Figure 3a) and urban (Figure 3b) regions. The shading in Figure 3 represents the constant surface flux that minimizes the residual of the model and the average monthly concentration in the respective region for a given combination of $C_{FT}$ and $C_{UW}$, where blue colors indicate a negative (deposition) flux, and reds indicate a positive (emission) flux. The transition between positive and negative fluxes occurs at lower $C_{FT}$ and $C_{UW}$ for the rural case than the urban case, and in both cases follows a slope that suggests greater sensitivity to $C_{UW}$ than $C_{FT}$ at both sites. In both regions, larger emission fluxes are required when boundary concentrations are low, while larger deposition fluxes are required when boundary concentrations are high.

Observational constraints can be used to identify reasonable areas of the solution spaces. For instance, if the midday convergence of $Hg^0$ concentrations in June is driven by the entrainment of free tropospheric air during PBL growth, then the midday extrema in rural and urban sites should approach the average regional value of $C_{FT}$. This allows us to ignore regions of the solution space where $C_{FT}$ is smaller than 1.25 ng $m^{-3}$ or larger than 1.55 ng $m^{-3}$ (Figure 3). We further constrain the reasonable solution space by selecting areas where the diel concentration amplitude simulated by the box model is within 50% of the average observed diel amplitude, which is indicated by the dashed outlined regions (Figure 3). Finally, we restrict the observationally-constrained solution space to negative values for the rural region and positive values for the urban region based on source and sink behavior established by existing literature[22,30]. The final observationally-constrained solution space for the rural region includes $C_{UW}$ ranging from 1.0 to 1.5 ng $m^{-3}$, which covers optimal fluxes between 0 – -15 ng $m^{-2}$ $hr^{-1}$, while the urban case includes upwind concentrations from 1.3-1.9 ng $m^{-3}$ and average surface fluxes of 0-30 ng $m^{-2}$ $hr^{-1}$.

The observationally constrained solution spaces described above indicate that NEST underestimates transport fluxes in both rural and urban regions. We estimate $C_{FT}$, $C_{UW}$, and F for the NEST simulation following the approach described in supplemental section S6 and plot the location of this simulation within the solution space as the circular point in both panels of Figure 3. In the rural region, GEOS-Chem predicts a net average surface flux of -2.6 ng $m^{-2}$ $hr^{-1}$, which is consistent with the range of fluxes in the observationally constrained solution space. However, NEST predicts $C_{UW}$=1.06 ng $m^{-2}$ and $C_{FT}$=1.09 ng $m^{-2}$, which lie well outside of the observationally constrained solution space. Similarly, the NEST simulation predicts an average surface flux of 1.4

ng m$^{-2}$ hr$^{-1}$ for the urban region that is consistent with the constrained solution space but has boundary concentrations of $C_{UW}$=1.1 ng m$^{-3}$ and $C_{FT}$=1.1 ng m$^{-3}$, again lying well outside of the observationally constrained solution space. We discuss sensitivity simulations that explore this solution space in section 3.3.

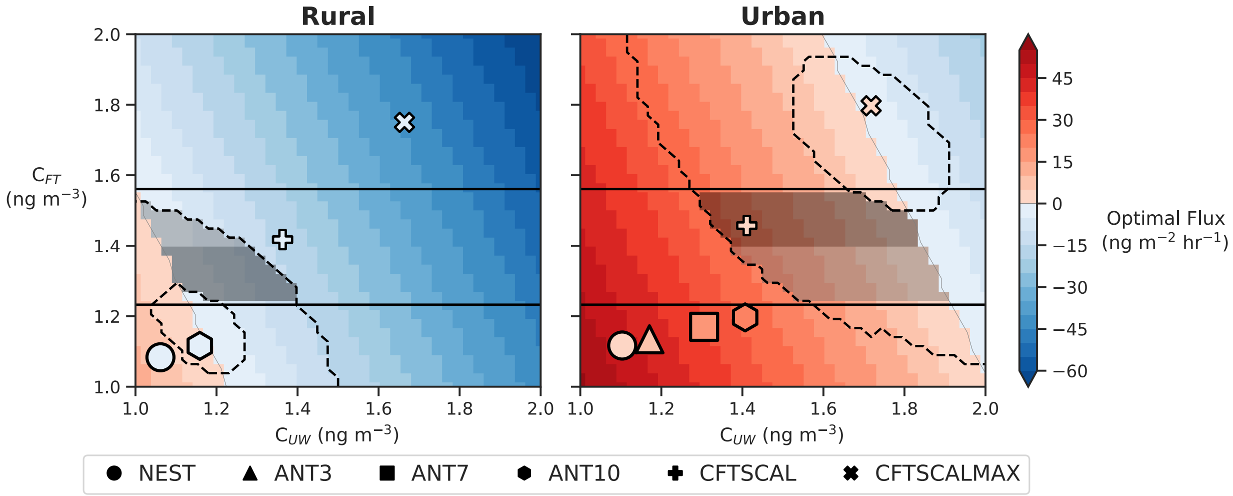

**Figure 3.** Solution space of the optimal flux for combinations of $C_{UW}$ and $C_{FT}$ from 1 ng m$^{-3}$ to 2 ng m$^{-3}$ in June for (a) rural and (b) urban regions. Horizontal solid lines refer to the likely bounds of $C_{FT}$, while dashed lines encompass the portion of the space where simulated diurnal amplitude is within 50% of the observed value. Gray shading outlines the observationally constrained solution space, with the heavy shading indicating the region with highest confidence. GEOS-Chem simulation results are overlaid based on estimated values $C_{FT}$ and $C_{UW}$ and F for the respective region.

We also use the box model to evaluate solution spaces for rural (Figure 4a) and urban (Figure 4b) sites in December. The threshold between positive and negative fluxes in the box model occurs at higher values of $C_{UW}$ in the rural region and lower values of $C_{UW}$ at the urban region. The flux threshold is also steeper than in June, suggesting a diminished influence of $C_{FT}$ that is consistent with increased stability and stronger horizontal advection typical during midlatitude winter

(Figures S2-S4). The observationally constrained solution space is smaller than in June, which is driven by the limited diel variation of concentrations in December. Interestingly, average midday concentrations (i.e., our $C_{FT}$ constraint) are notably higher in December at the rural sites but are only slightly higher at urban sites, suggesting that $C_{FT}$ varies spatially. As in June, the average net flux within each region suggested by NEST is consistent with the observationally constrained solution space in both rural and urban regions, however $C_{UW}$ and $C_{FT}$ are notably lower than those in the constrained space.

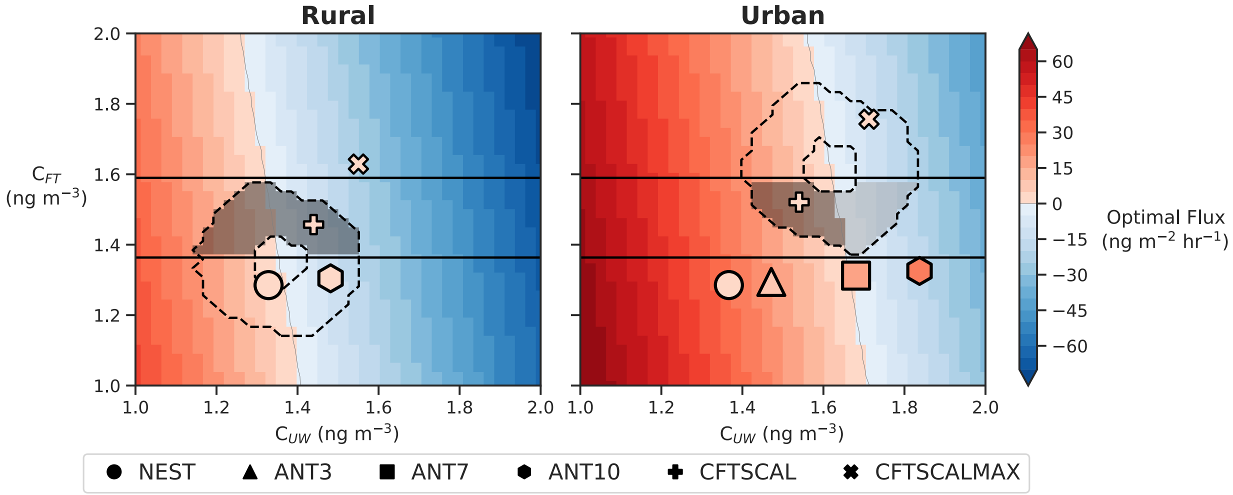

**Figure 4.** Solution space of the optimal flux for combinations of $C_{UW}$ and $C_{FT}$ from 1 ng m$^{-3}$ to 2 ng m$^{-3}$ in December for (a) rural and (b) urban regions. Horizontal solid lines refer to the likely bounds of $C_{FT}$, while dashed lines encompass the region of the space where simulated diurnal amplitude is within 50% of the observed value. Gray shading outlines the observationally constrained solution space, with the heavy shading indicating the region with highest confidence. GEOS-Chem simulation results are overlaid based on estimated values $C_{FT}$ and $C_{UW}$ and F for the respective region.

### 3.3. Impact of flux enhancement on diel variability

We evaluate a series of sensitivity simulations to determine whether enhancements to regional surface fluxes (i.e., F) or transport fluxes (i.e., $C_{FT}$ and $C_{UW}$) can allow GEOS-Chem to satisfy the observationally constrained solution space in June (Figure 3). We first evaluate the impact of regional surface flux enhancements using the ANT3, ANT7, and ANT10 simulations. These simulations scale anthropogenic emissions throughout the northeastern US (Figure 1, solid box), meaning that F, $C_{UW}$, and $C_{FT}$ may be sensitive to changes (see supplemental section S6). We find that enhancing anthropogenic emissions by a factor of ten has little effect on the net regional flux in the rural region since there are limited anthropogenic emissions in this area (Figure 1) and surface fluxes are dominated by vegetative uptake. However, we find that this emission enhancement does lead to a 9% and 3% increase in the rural $C_{UW}$ and $C_{FT}$, respectively. The same factor of ten anthropogenic emission enhancement has a larger effect on the net regional flux (encompassing all emission and deposition processes) in the urban region, increasing the net flux by a factor of 17 (23.9 ng $m^{-2}$ $hr^{-1}$) and $C_{UW}$ and $C_{FT}$ by 27% and 7%, respectively. However, the $C_{UW}$ and $C_{FT}$ increases caused by this regional emission enhancement are insufficient to satisfy the observationally constrained solution space.

We also evaluate the impact of enhancements to regional $C_{FT}$ in June using the CFTSCAL and CFTSCALMAX simulations in this region (Figure 3). $C_{UW}$ is remarkably sensitive to $C_{FT}$ in both urban and rural regions, and net surface fluxes are not notably impacted in either simulation. Our $C_{FT}$ enhancements overshoot the constrained solution space for the rural region, however the strong linear response of the two simulations suggest that a value of $C_{FT}$ that is higher than NEST but lower than CFTSCAL in this region would move GEOS-Chem into the observationally constrained solution space. We observe a similar linear response to $C_{FT}$ enhancements in the urban region and find that the CFTSCAL simulation moves GEOS-Chem into the optimally constrained solution space, albeit with a regional surface flux that is inconsistent with the underlying solution space.

We find that regional anthropogenic emission enhancements are also insufficient for GEOS-Chem to satisfy the observationally constrained solution space in December. Additionally, we find that $C_{FT}$ has lower sensitivity to regional emission enhancements in December than in June, which is consistent with increased atmospheric stability in winter. As in June, $C_{FT}$ enhancements also influence $C_{UW}$, with CFTSCAL shifting GEOS-Chem to the constrained solution space in rural and urban areas. However, net GEOS-Chem fluxes do not correspond with the underlying solution space, having the opposite sign in the rural case (Figure 4a) and being too weak in the urban case (Figure 4b).

We evaluate the impact of enhancements to regional emissions or $C_{FT}$ at urban and rural sites on diel variability in both June and December and find that neither are sufficient to reproduce observed patterns (Figures 5, S18). For instance, the regional emission enhancement explored in the ANT7 simulation increased F, $C_{UW}$, and $C_{FT}$ in the urban region (Figure 3), which we find results in a stronger diel variation with amplitude that is comparable to observations in June (Figure 5a), though this same simulation overestimates diel amplitude in December (Figure 5b). Meanwhile, the CFTSCAL simulation increases transport fluxes without affecting regional surface fluxes, which results in a uniform enhancement to concentrations in both June and December (Figures 5c and 5d, respectively, Figure S18). This adjustment does not notably affect the concentration difference between rural and urban concentrations but has a strong impact on overall average concentrations. This highlights that neither regional emission enhancements nor $C_{FT}$ enhancements alone can allow GEOS-Chem to reproduce observed spatial and diel variability.

Instead, our modeling results demonstrate the complementary effects of these key fluxes, with surface fluxes primarily responsible for setting the amplitude of diel variations and $C_{FT}$ primarily responsible for setting the daytime convergence point of concentrations.

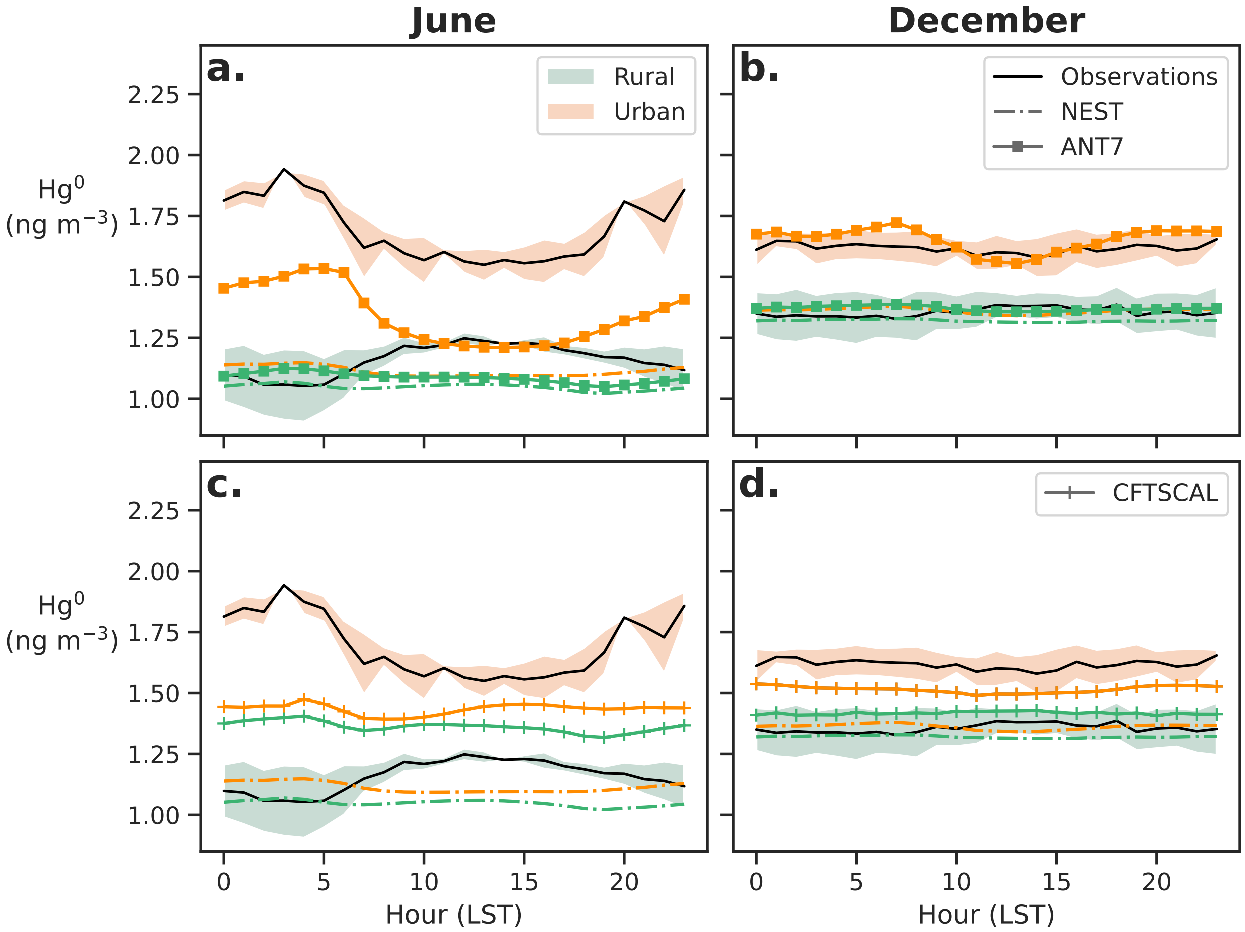

**Figure 5.** Comparison of diel variation of average regional observations (black lines) and NEST simulations with respective predictions from the ANT7 (panels a and b) and CFTSCAL (panels c and d) sensitivity simulations. Green and orange represent rural and urban regions, respectively. Colored shading around regionally averaged observations represents the hourly average concentrations at the two sites within the respective region.

It is worth noting that each GEOS-Chem simulation fails to reproduce the nocturnal concentration minimum observed at rural sites. This is likely caused by the existing parameterization of $Hg^0$ uptake in GEOS-Chem which is largely driven by incoming solar radiation[6], preventing the simulation of net nocturnal uptake suggested by recent observations[22,25,26,36]. As a result, modeled concentrations remain constant or increase slightly overnight, unlike declines implied by observations.

### 3.4. Implications for atmospheric modeling and monitoring

Our analysis shows that diel variations of $Hg^0$ concentrations can serve as a useful constraint on magnitude and temporal variation of regional free tropospheric concentrations, for which there are limited observations. The ranges of $C_{FT}$ suggested by midday concentrations at urban and rural sites in June and December (1.25-1.55 ng $m^{-3}$ and 1.35-1.60 ng $m^{-3}$, respectively) are consistent with vertical profiles taken during an aircraft campaign in Tennessee in 2012 and 2013[37], where summertime concentrations in the lower 5 km of the atmosphere ranged between 1.0-1.4 ng $m^{-3}$ in June and 1.25-1.6 ng $m^{-3}$ in November and January. Given the expense of aircraft-based measurements, we argue that existing ground-based measurements can be used to identify a useful estimate of this concentration, which we show is critical for accurate representation of spatial and temporal variability in CTMs.

The spatial and temporal variability of surface $Hg^0$ concentrations at regional scales can be largely explained by processes that should be able to be captured by global CTMs. Our simple modeling exercise demonstrates that the daily variation of concentrations can be explained by the interaction of regional surface fluxes and transport fluxes, rather than previously hypothesized short-term reservoirs or local redox chemistry, which we would not expect to capture with currently available CTMs. Therefore, we suggest that diel variability can serve as an additional constraint to evaluate the mechanistic performance of CTMs.

The biases that we observe in urban and rural regions in our GEOS-Chem simulations imply that the free tropospheric burden of $Hg^0$ in GEOS-Chem is underestimated, which may be addressed by enhancing key global sources (emissions, reduction of $Hg^{II}$) or reducing key global sinks (deposition, oxidation of $Hg^0$). While enhancing $Hg^{II}$ reduction or reducing $Hg^0$ oxidation could increase free tropospheric burdens of $Hg^0$, Shah et al.[8] found that the chemical mechanism currently used in GEOS-Chem also underestimates $Hg^{II}$ loadings in the free troposphere, leading to underestimates of wet deposition. $Hg^0$ underestimates are also unlikely to be driven by excessive $Hg^0$ vegetative uptake, as a subsequent update to the GEOS-Chem model using direct observational constraints on this flux increased simulated annual $Hg^0$ deposition by 84%[6] when compared to the Shah et al. model.

Given these constraints, broadly distributed emission enhancements are the most likely explanation for the underestimate of the free tropospheric burden. We evaluate the impact of emission enhancements across broader spatial scales using the ANT3-ENA, ANT7-ENA, and ANT10-ENA sensitivity simulations, where emissions are scaled across eastern North America (Figure 1, Figures S16-S17). Using the strong linear response of $C_{FT}$ to regional emission enhancements, we calculate the net regional flux required to reproduce the lower bound and central estimate of $C_{FT}$ in June (1.25 and 1.45 ng $m^{-3}$, respectively). For sensitivity simulations where emission enhancements are only applied to the northeast US, emissions would need to be enhanced by a factor of 16 and 32 to reach these $C_{FT}$ values, while emissions would need to be enhanced by a factor of 8 and 16 if enhancements are applied across eastern North America. Given the unlikely emission enhancements required over the northeastern US or eastern North America to satisfy observational constraints on $C_{FT}$, along with the associated unlikely enhancements to $C_{UW}$, smaller emission enhancements across continental or hemispheric scales are likely required.

Our findings demonstrate that diel variability can serve as a critical constraint on tropospheric Hg loadings in CTMs that are used to evaluate environmental policy effectiveness, motivating continued support of temporally resolved Hg monitoring networks.

## CODE AND DATA AVAILABILITY

All code and model data required to reproduce the results presented in this study are published on Zenodo (10.5281/zenodo.20432685)[38].

## ASSOCIATED CONTENT

*Supporting information*. Further supporting information can be found in the attached pdf.

## AUTHOR INFORMATION

### Corresponding Author

* Eric Roy – Department of Earth, Atmospheric, and Planetary Sciences, Massachusetts Institute of Technology, Cambridge, MA, 02139, USA; https://orcid.org/0000-0002-3077-8011; Email: emroy@mit.edu

## ACKNOWLEDGMENT

We would like to acknowledge helpful conversations with Yuying Cui, Lexia Cicone, and Connor Olsen. This research was made possible by United States National Science Foundation grant #1924148, the MIT Department of Earth, Atmospheric, and Planetary Sciences Charney Fellowship. This publication was made possible by the generous support of the Government of Portugal through the Portuguese Foundation for International Cooperation in Science, Technology and Higher Education and was undertaken in MIT Portugal Program.

## GRAPHICAL ABSTRACT

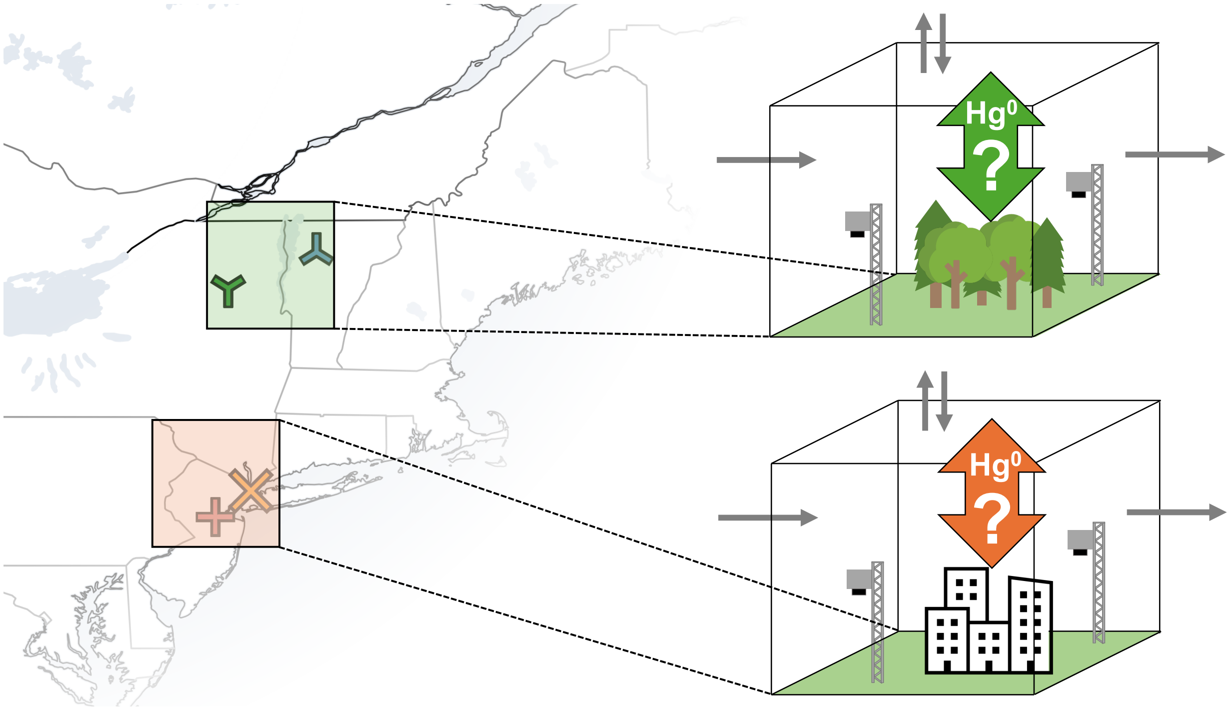

## REFERENCES

(1) Basu, N.; Bastiansz, A.; Dórea, J. G.; Fujimura, M.; Horvat, M.; Shroff, E.; Weihe, P.; Zastenskaya, I. Our Evolved Understanding of the Human Health Risks of Mercury. *Ambio* **2023**, *52* (5), 877–896. https://doi.org/10.1007/s13280-023-01831-6.

(2) Hsu-Kim, H.; Eckley, C. S.; Achá, D.; Feng, X.; Gilmour, C. C.; Jonsson, S.; Mitchell, C. P. J. Challenges and Opportunities for Managing Aquatic Mercury Pollution in Altered Landscapes. *Ambio* **2018**, *47* (2), 141–169. https://doi.org/10.1007/s13280-017-1006-7.

(3) Driscoll, C. T.; Mason, R. P.; Chan, H. M.; Jacob, D. J.; Pirrone, N. Mercury as a Global Pollutant: Sources, Pathways, and Effects. *Environ. Sci. Technol.* **2013**, *47* (10), 4967–4983. https://doi.org/10.1021/es305071v.

(4) Amos, H. M.; Jacob, D. J.; Streets, D. G.; Sunderland, E. M. Legacy Impacts of All-Time Anthropogenic Emissions on the Global Mercury Cycle. *Glob. Biogeochem. Cycles* **2013**, *27* (2), 410–421. https://doi.org/10.1002/gbc.20040.

(5) Geyman, B. M.; Streets, D. G.; Olson, C. I.; Thackray, C. P.; Olson, C. L.; Schaefer, K.; Krabbenhoft, D. P.; Sunderland, E. M. Cumulative Anthropogenic Impacts of Past and Future Emissions and Releases on the Global Mercury Cycle. *Environ. Sci. Technol.* **2025**, *59* (17), 8578–8590. https://doi.org/10.1021/acs.est.4c13434.

(6) Feinberg, A.; Dlamini, T.; Jiskra, M.; Shah, V.; Selin, N. E. Evaluating Atmospheric Mercury (Hg) Uptake by Vegetation in a Chemistry-Transport Model. *Environ. Sci. Process. Impacts* **2022**, *24* (9), 1303–1318. https://doi.org/10.1039/D2EM00032F.

(7) Horowitz, H. M.; Jacob, D. J.; Zhang, Y.; Dibble, T. S.; Slemr, F.; Amos, H. M.; Schmidt, J. A.; Corbitt, E. S.; Marais, E. A.; Sunderland, E. M. A New Mechanism for Atmospheric Mercury Redox Chemistry: Implications for the Global Mercury Budget. *Atmospheric Chem. Phys.* **2017**, *17* (10), 6353–6371. https://doi.org/10.5194/acp-17-6353-2017.

(8) Shah, V.; Jacob, D. J.; Thackray, C. P.; Wang, X.; Sunderland, E. M.; Dibble, T. S.; Saiz-Lopez, A.; Černušák, I.; Kellö, V.; Castro, P. J.; Wu, R.; Wang, C. Improved Mechanistic Model of the Atmospheric Redox Chemistry of Mercury. *Environ. Sci. Technol.* **2021**, *55* (21), 14445–14456. https://doi.org/10.1021/acs.est.1c03160.

(9) Zhou, J.; Obrist, D.; Dastoor, A.; Jiskra, M.; Ryjkov, A. Vegetation Uptake of Mercury and Impacts on Global Cycling. *Nat. Rev. Earth Environ.* **2021**, *2* (4), 269–284. https://doi.org/10.1038/s43017-021-00146-y.

(10) Gustin, M. S.; Dunham-Cheatham, S. M.; Osterwalder, S.; Magand, O.; Dommergue, A. What Is the Utility of Measuring Gaseous HgII Dry Deposition Using Aerohead Samplers?: A Review. *Sci. Total Environ.* **2024**, *907*, 167895. https://doi.org/10.1016/j.scitotenv.2023.167895.

(11) Prestbo, E. M.; Gay, D. A. Wet Deposition of Mercury in the U.S. and Canada, 1996–2005: Results and Analysis of the NADP Mercury Deposition Network (MDN). *Atmos. Environ.* **2009**, *43* (27), 4223–4233. https://doi.org/10.1016/j.atmosenv.2009.05.028.

(12) Saiz-Lopez, A.; Sitkiewicz, S. P.; Roca-Sanjuán, D.; Oliva-Enrich, J. M.; Dávalos, J. Z.; Notario, R.; Jiskra, M.; Xu, Y.; Wang, F.; Thackray, C. P.; Sunderland, E. M.; Jacob, D. J.; Travnikov, O.; Cuevas, C. A.; Acuña, A. U.; Rivero, D.; Plane, J. M. C.; Kinnison, D. E.; Sonke, J. E. Photoreduction of Gaseous Oxidized Mercury Changes Global Atmospheric Mercury Speciation, Transport and Deposition. *Nat. Commun.* **2018**, *9* (1), 4796. https://doi.org/10.1038/s41467-018-07075-3.

(13) Gay, D. A.; Schmeltz, D.; Prestbo, E.; Olson, M.; Sharac, T.; Tordon, R. The Atmospheric Mercury Network: Measurement and Initial Examination of an Ongoing Atmospheric Mercury Record across North America. *Atmospheric Chem. Phys.* **2013**, *13* (22), 11339–11349. https://doi.org/10.5194/acp-13-11339-2013.

(14) Sprovieri, F.; Pirrone, N.; Bencardino, M.; D'Amore, F.; Carbone, F.; Cinnirella, S.; Mannarino, V.; Landis, M.; Ebinghaus, R.; Weigelt, A.; Brunke, E.-G.; Labuschagne, C.; Martin, L.; Munthe, J.; Wängberg, I.; Artaxo, P.; Morais, F.; Barbosa, H. D. M. J.; Brito, J.; Cairns, W.; Barbante, C.; Diéguez, M. D. C.; Garcia, P. E.; Dommergue, A.; Angot, H.; Magand, O.; Skov, H.; Horvat, M.; Kotnik, J.; Read, K. A.; Neves, L. M.; Gawlik, B. M.; Sena, F.; Mashyanov, N.; Obolkin, V.; Wip, D.; Feng, X. B.; Zhang, H.; Fu, X.; Ramachandran, R.; Cossa, D.; Knoery, J.; Marusczak, N.; Nerentorp, M.; Norstrom, C. Atmospheric Mercury Concentrations Observed at Ground-Based Monitoring Sites Globally Distributed in the Framework of the GMOS Network. *Atmospheric Chem. Phys.* **2016**, *16* (18), 11915–11935. https://doi.org/10.5194/acp-16-11915-2016.

(15) Stamenkovic, J.; Lyman, S.; Gustin, M. S. Seasonal and Diel Variation of Atmospheric Mercury Concentrations in the Reno (Nevada, USA) Airshed. *Atmos. Environ.* **2007**, *41* (31), 6662–6672. https://doi.org/10.1016/j.atmosenv.2007.04.015.

(16) Mao, H.; Cheng, I.; Zhang, L. Current Understanding of the Driving Mechanisms for Spatiotemporalvariations of Atmospheric Speciated Mercury: A Review. *Atmospheric Chem. Phys.* **2016**, *16* (20), 12897–12924. https://doi.org/10.5194/acp-16-12897-2016.

(17) Lyman, S. N.; Elgiar, T.; Gustin, M. S.; Dunham-Cheatham, S. M.; David, L. M.; Zhang, L. Evidence against Rapid Mercury Oxidation in Photochemical Smog. *Environ. Sci. Technol.* **2022**, *56* (16), 11225–11235. https://doi.org/10.1021/acs.est.2c02224.

(18) Lan, X.; Talbot, R.; Castro, M.; Perry, K.; Luke, W. Seasonal and Diurnal Variations of Atmospheric Mercury across the US Determined from AMNet Monitoring Data.

*Atmospheric Chem. Phys.* **2012**, *12* (21), 10569–10582. https://doi.org/10.5194/acp-12-10569-2012.

(19) Nair, U. S.; Wu, Y.; Walters, J.; Jansen, J.; Edgerton, E. S. Diurnal and Seasonal Variation of Mercury Species at Coastal-Suburban, Urban, and Rural Sites in the Southeastern United States. *Atmos. Environ.* **2012**, *47*, 499–508. https://doi.org/10.1016/j.atmosenv.2011.09.056.

(20) Roy, E. M.; Zhou, J.; Wania, F.; Obrist, D. Use of Atmospheric Concentrations and Passive Samplers to Assess Surface-Atmosphere Exchange of Gaseous Mercury in Forests. *Chemosphere* **2023**, *341*, 140113. https://doi.org/10.1016/j.chemosphere.2023.140113.

(21) Jiskra, M.; Sonke, J. E.; Obrist, D.; Bieser, J.; Ebinghaus, R.; Myhre, C. L.; Pfaffhuber, K. A.; Wängberg, I.; Kyllönen, K.; Worthy, D.; Martin, L. G.; Labuschagne, C.; Mkololo, T.; Ramonet, M.; Magand, O.; Dommergue, A. A Vegetation Control on Seasonal Variations in Global Atmospheric Mercury Concentrations. *Nat. Geosci.* **2018**, *11* (4), 244–250. https://doi.org/10.1038/s41561-018-0078-8.

(22) Obrist, D.; Roy, E. M.; Harrison, J. L.; Kwong, C. F.; Munger, J. W.; Moosmüller, H.; Romero, C. D.; Sun, S.; Zhou, J.; Commane, R. Previously Unaccounted Atmospheric Mercury Deposition in a Midlatitude Deciduous Forest. *Proc. Natl. Acad. Sci.* **2021**, *118* (29), e2105477118. https://doi.org/10.1073/pnas.2105477118.

(23) St. Louis, V. L.; Graydon, J. A.; Lehnherr, I.; Amos, H. M.; Sunderland, E. M.; St. Pierre, K. A.; Emmerton, C. A.; Sandilands, K.; Tate, M.; Steffen, A.; Humphreys, E. R. Atmospheric Concentrations and Wet/Dry Loadings of Mercury at the Remote Experimental Lakes Area, Northwestern Ontario, Canada. *Environ. Sci. Technol.* **2019**, *53* (14), 8017–8026. https://doi.org/10.1021/acs.est.9b01338.

(24) Howard, D.; Edwards, G. C. Mercury Fluxes over an Australian Alpine Grassland and Observation of Nocturnal Atmospheric Mercury Depletion Events. *Atmospheric Chem. Phys.* **2018**, *18* (1), 129–142. https://doi.org/10.5194/acp-18-129-2018.

(25) Zhou, J.; Bollen, S. W.; Roy, E. M.; Hollinger, D. Y.; Wang, T.; Lee, J. T.; Obrist, D. Comparing Ecosystem Gaseous Elemental Mercury Fluxes over a Deciduous and Coniferous Forest. *Nat. Commun.* **2023**, *14* (1), 2722. https://doi.org/10.1038/s41467-023-38225-x.

(26) Denzler, B.; Eugster, W.; Bogdal, C.; Bishop, K.; Buchmann, N.; Hungerbühler, K.; Osterwalder, S. Uptake of Gaseous Elemental Mercury by a Rainforest: Insights from a Tropical Glasshouse Used as a Dynamic Flux Chamber. *Environ. Sci. Technol.* **2025**, *59* (35), 18675–18686. https://doi.org/10.1021/acs.est.5c05823.

(27) Denzler, B.; Bogdal, C.; Kern, C.; Tobler, A.; Huo, J.; Hungerbühler, K. Urban Source Term Estimation for Mercury Using a Boundary-Layer Budget Method. *Atmos Chem Phys* **2019**.

(28) Gustin, M. S.; Dunham-Cheatham, S. M.; Lyman, S.; Horvat, M.; Gay, D. A.; Gačnik, J.; Gratz, L.; Kempkes, G.; Khalizov, A.; Lin, C.-J.; Lindberg, S. E.; Lown, L.; Martin, L.; Mason, R. P.; MacSween, K.; Vijayakumaran Nair, S.; Nguyen, L. S. P.; O'Neil, T.; Sommar, J.; Weiss-Penzias, P.; Zhang, L.; Živković, I. Measurement of Atmospheric Mercury: Current Limitations and Suggestions for Paths Forward. *Environ. Sci. Technol.* **2024**, *58* (29), 12853–12864. https://doi.org/10.1021/acs.est.4c06011.

(29) US Environmental Protection Agency. USEPA 2020 National Emissions Inventory, 2023.

(30) Aucott, M. L.; Caldarelli, A. D.; Zsolway, R. R.; Pietarinen, C. B.; England, R. Ambient Elemental, Reactive Gaseous, and Particle-Bound Mercury Concentrations in New Jersey, U.S.: Measurements and Associations with Wind Direction. *Environ. Monit. Assess.* **2009**, *158* (1–4), 295–306. https://doi.org/10.1007/s10661-008-0583-0.

(31) Steenhuisen, F.; Wilson, S. J. Development and Application of an Updated Geospatial Distribution Model for Gridding 2015 Global Mercury Emissions. *Atmos. Environ.* **2019**, *211*, 138–150. https://doi.org/10.1016/j.atmosenv.2019.05.003.
(32) Li, D. AMDAR_BL_PBLH_DATASET, 2020. https://doi.org/10.5281/ZENODO.3934377.
(33) Zhang, Y.; Sun, K.; Gao, Z.; Pan, Z.; Shook, M. A.; Li, D. Diurnal Climatology of Planetary Boundary Layer Height Over the Contiguous United States Derived From AMDAR and Reanalysis Data. *J. Geophys. Res. Atmospheres* **2020**, *125* (20), e2020JD032803. https://doi.org/10.1029/2020JD032803.
(34) Seinfeld, J. H.; Pandis, S. N. *Atmospheric Chemistry and Physics: From Air Pollution to Climate Change*, Third edition.; John Wiley & Sons: Hoboken, New Jersey, 2016.
(35) Angot, H.; Rutkowski, E.; Sargent, M.; Wofsy, S. C.; Hutyra, L. R.; Howard, D.; Obrist, D.; Selin, N. E. Atmospheric Mercury Sources in a Coastal-Urban Environment: A Case Study in Boston, Massachusetts, USA. *Environ. Sci. Process. Impacts* **2021**, *23* (12), 1914–1929. https://doi.org/10.1039/D1EM00253H.
(36) Khan, T. R.; Obrist, D.; Agnan, Y.; Selin, N. E.; Perlinger, J. A. Atmosphere-Terrestrial Exchange of Gaseous Elemental Mercury: Parameterization Improvement through Direct Comparison with Measured Ecosystem Fluxes. *Environ. Sci. Process. Impacts* **2019**, *21* (10), 1699–1712. https://doi.org/10.1039/C9EM00341J.
(37) Brooks, S.; Ren, X.; Cohen, M.; Luke, W.; Kelley, P.; Artz, R.; Hynes, A.; Landing, W.; Martos, B. Airborne Vertical Profiling of Mercury Speciation near Tullahoma, TN, USA. *Atmosphere* **2014**, *5* (3), 557–574. https://doi.org/10.3390/atmos5030557.
(38) Roy, E.; Selin, N. Data and Code for Publication: “Spatially and Temporally Dense Measurements Reveal Meteorological Driver of Atmospheric Mercury Variability,” 2026. https://doi.org/10.5281/ZENODO.20432685.

**SUPPORTING INFORMATION**

# Spatially and temporally dense measurements reveal meteorological driver of atmospheric mercury variability

Eric M. Roy[1,2]*, David A. Gay[3], Noelle E. Selin[1,2,4]

[1]Department of Earth, Atmospheric, and Planetary Sciences, Massachusetts Institute of Technology, Cambridge, MA, USA

[2]Center for Sustainability Science and Strategy, Massachusetts Institute of Technology, Cambridge, MA, USA

[3]National Atmospheric Deposition Program, Wisconsin State Laboratory of Hygiene, University of Wisconsin Madison, Madison, WI, USA

[4]Institute for Data, Systems, and Society, Massachusetts Institute of Technology, Cambridge, MA, USA

*Corresponding author: Eric M. Roy, Email: emroy@mit.edu

Number of pages: 14

Number of sections: 7

Number of tables: 1

Number of figures: 18

## Section S1. $Hg^0$ Concentrations at Elizabeth, NJ (NJ54)

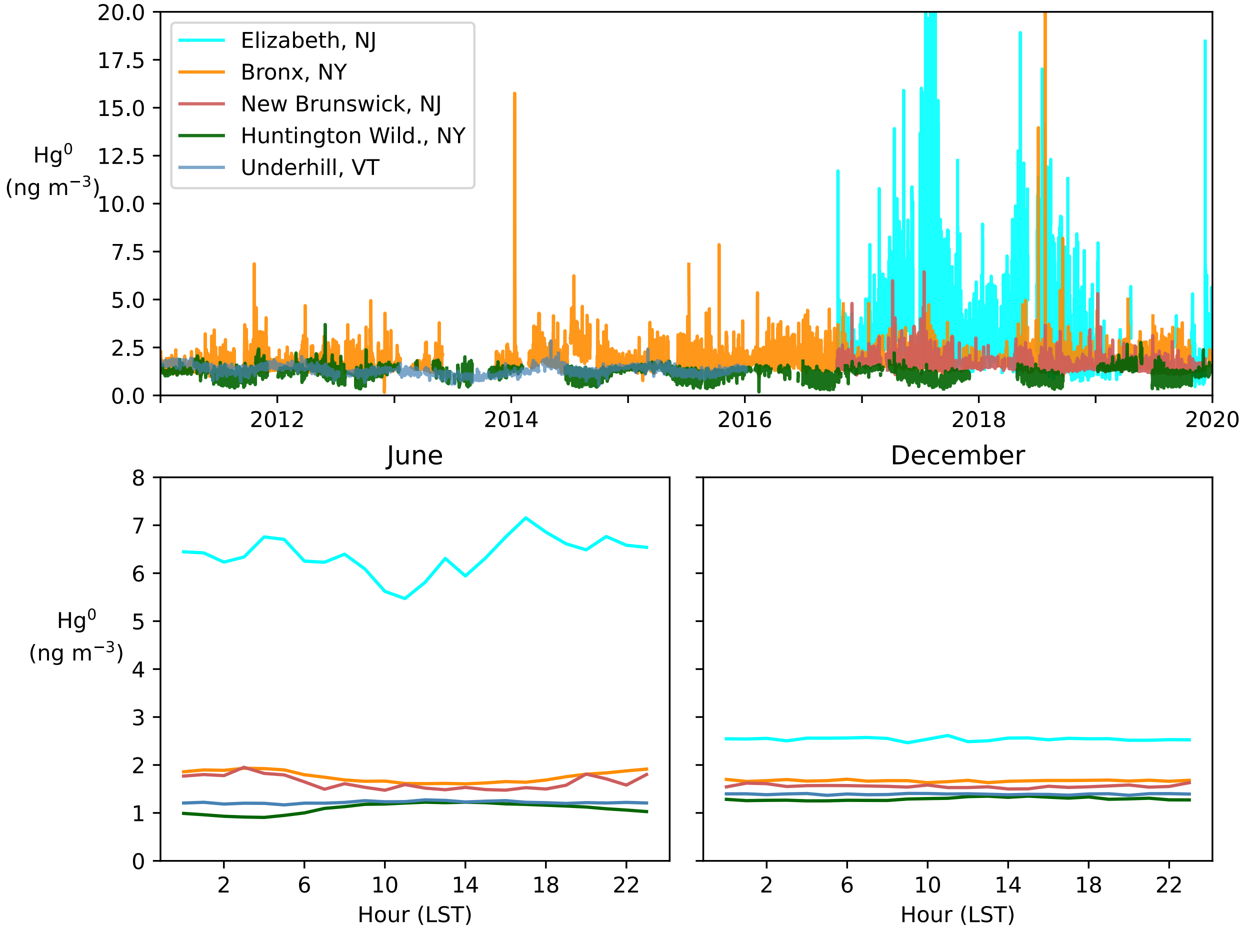

**Figure S1.** (top) Hourly concentrations at the four sites of interest, here including measurements at Elizabeth, NJ. Concentrations are notably higher at this site, even compared to The Bronx and New Brunswick. Average concentrations for each hour of the day during June (bottom left) are more than twice as high as other urban sites. Hourly average concentrations during December do not exhibit any notable diel cycle but remain notably higher than all other sites, further underscoring the likelihood that local sources exert a dominating influence on variability.

## Section S2. Evaluation of PBLH data used to drive boundary layer box model

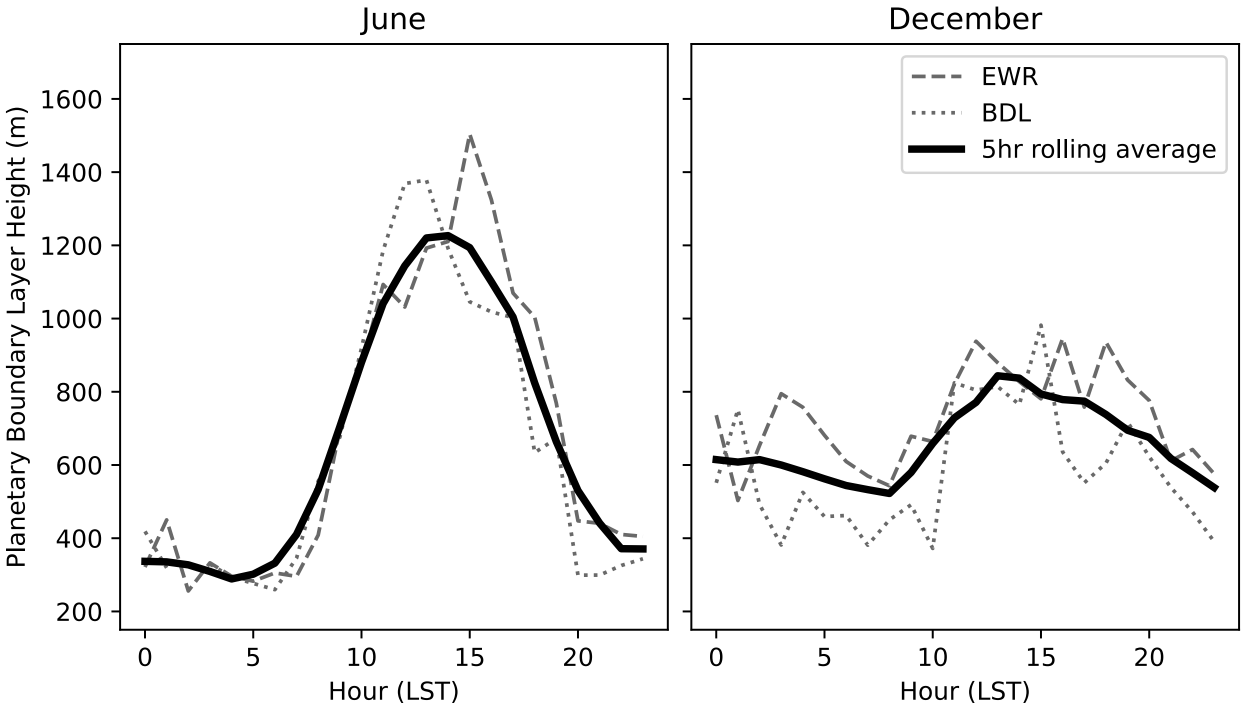

**Figure S2.** Comparison of PBLH from hourly data from Newark-Liberty International Airport (EWR) and Bradley International Airport (BDL) for June (left) and December (right) 2017. Average monthly PBLH is defined as the five-hour centered rolling average of these data, plotted as the solid black curve.

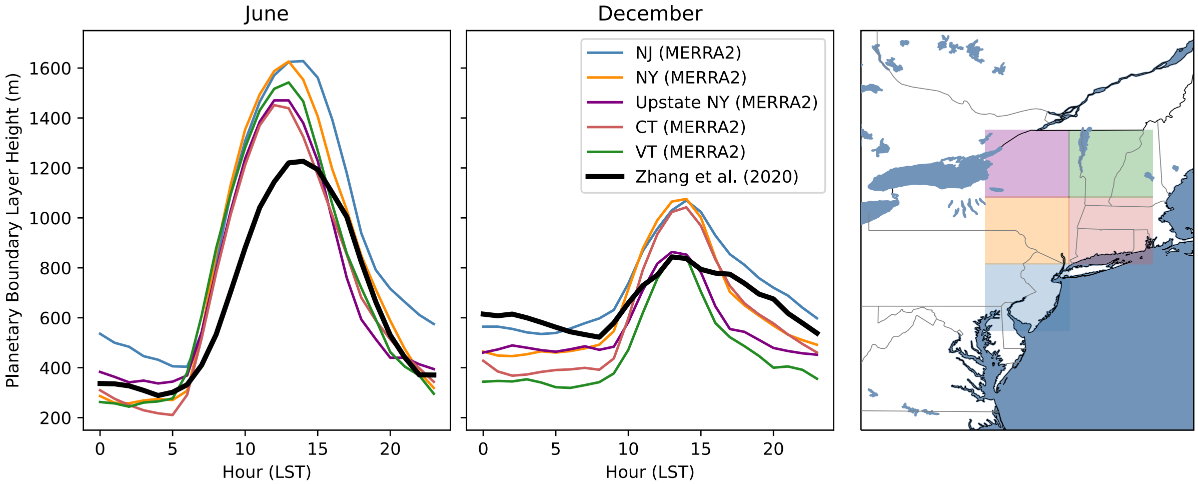

**Figure S3.** Average diurnal variation of planetary boundary layer height (PBLH) in smoothed observationally derived dataset and MERRA2 reanalysis for June (left) and December (middle). The regions represented by each of the MERRA2 variations are shown in the right panel. Observationally derived PBLH is similar in magnitude and diel variation to MERRA2, which does not exhibit large spatial variation. In June, observationally derived profile is slightly lower than MERRA2 during midday.

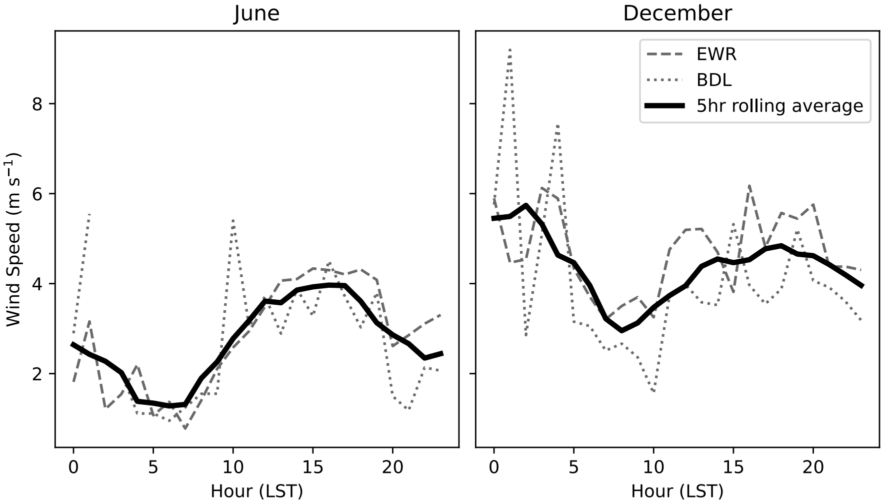

**Figure S4.** Comparison of average windspeed within the PBL from hourly data from Newark-Liberty International Airport (EWR) and Bradley International Airport (BDL) for June (left) and December (right) 2017. Average monthly windspeed for the box model ($u$) is defined as the five-hour centered rolling average of these data. Winds are notably higher in December than in June, which is consistent with seasonal shifts of synoptic-scale weather patterns in the northeastern US.

## Section S3. Comparison of calibrated solution spaces with constant and temporally varying surface fluxes

Here, we demonstrate the negligible effect of allowing fluxes to vary temporally in our box model optimization to justify our use of constant fluxes in the main text. Over a limited number of combinations of $C_{FT}$ and $C_{UW}$, we recalculate the optimal average flux in our box model when driven by a constant flux. Then, across the same domain, we repeat the same optimization while allowing the flux to vary in four hour segments. We find that average net fluxes are similar in both cases at both rural and urban sites (Figures S5, S7). We find that diurnally varying fluxes do reduce the difference between the observed diel variation when compared to the constant flux cases by reducing the extent of extremes (right panels, Figures S6 and S8). However, this is likely driven by overfitting, as we observe that this agreement is achieved unreasonably sharp temporal shifts in Hg fluxes that are not supported by any existing mechanisms (left panels, Figures S6 and S8). Furthermore, the diel average of these fluxes are similar in magnitude to the optimal fluxes obtained using constant values. The close correspondence of average fluxes from both methods, coupled with our overarching goal of finding the dominant drivers of diel variations in this region support our choice to drive our box model with temporally invariant surface fluxes in the main text.

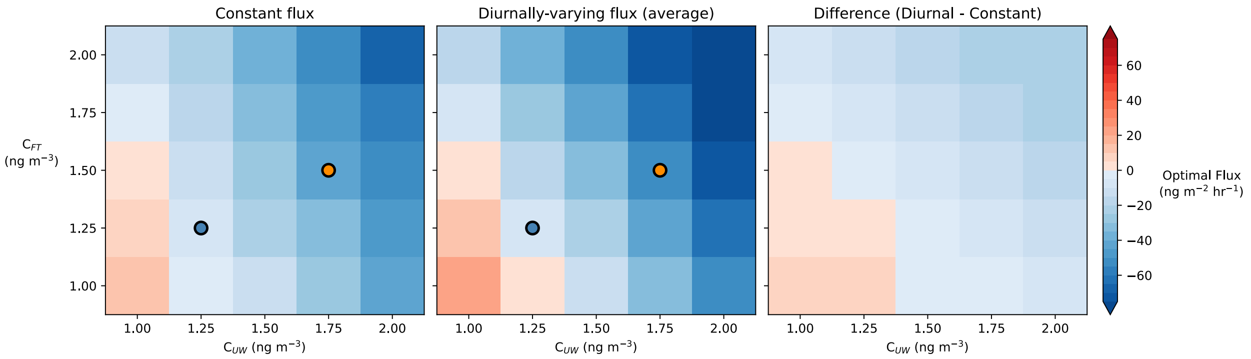

**Figure S5.** Comparison of optimal average surface flux at the rural sites predicted by box model with constant surface flux (left) or a diurnally-varying surface fluxes (middle), and their difference (right). Both approaches result in a qualitatively similar solution space, where the diurnally varying flux approach predicts larger average positive and negative fluxes. Blue and orange points represent concentration and flux combinations that are further explored in figure S6.

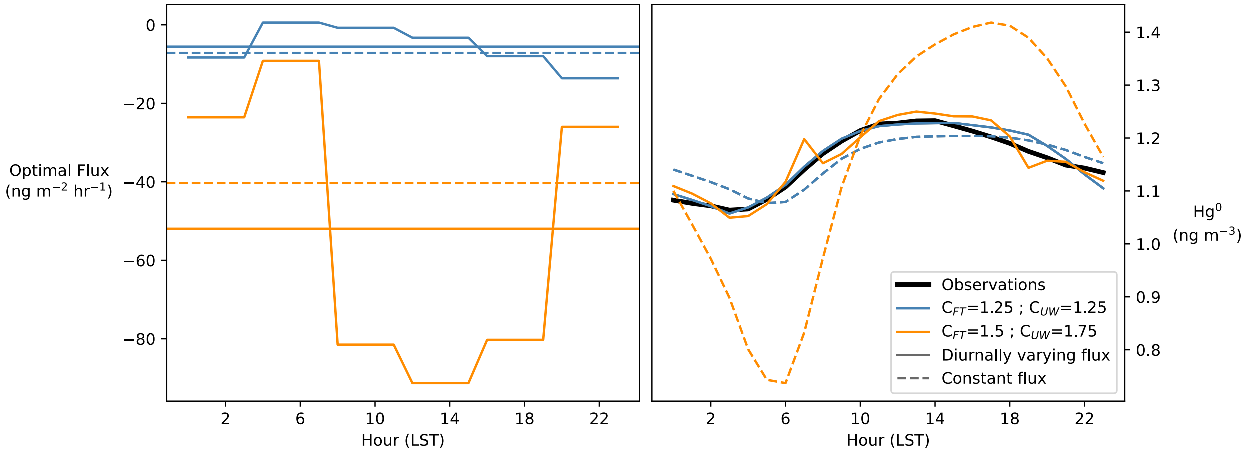

**Figure S6.** Comparison of the optimal constant flux and optimal diurnally varying flux for the two combinations of CFT and CUW shown in figure S5 (left) and the respective concentration variation (right). In both cases, the constant flux is similar in magnitude to the average of the temporally varying flux. The temporally varying flux simulates concentrations that lie closer to observations than the constant flux case.

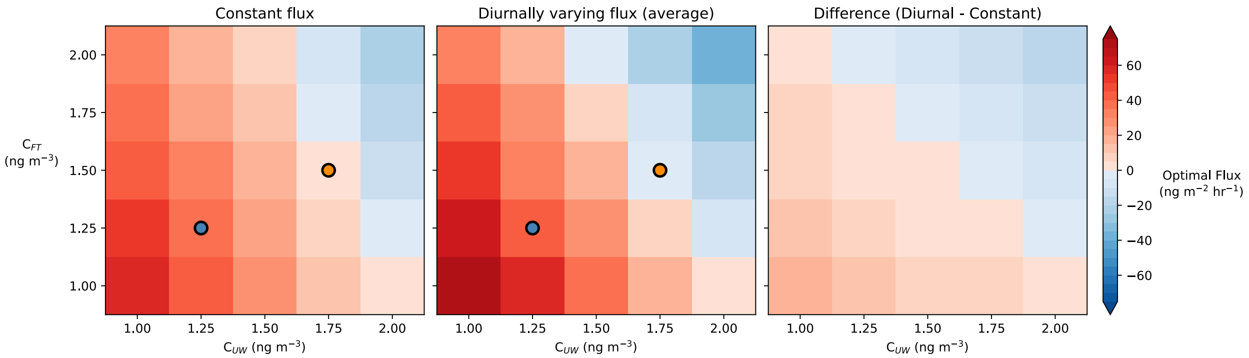

**Figure S7.** Comparison of optimal average surface flux at the urban sites predicted by box model with constant surface flux (left) or a diurnally-varying surface fluxes (middle), and their difference (right). Both approaches result in a qualitatively similar solution space, where the diurnally varying flux approach predicts larger average positive and negative fluxes. Blue and orange points represent concentration and flux combinations that are further explored in figure S8.

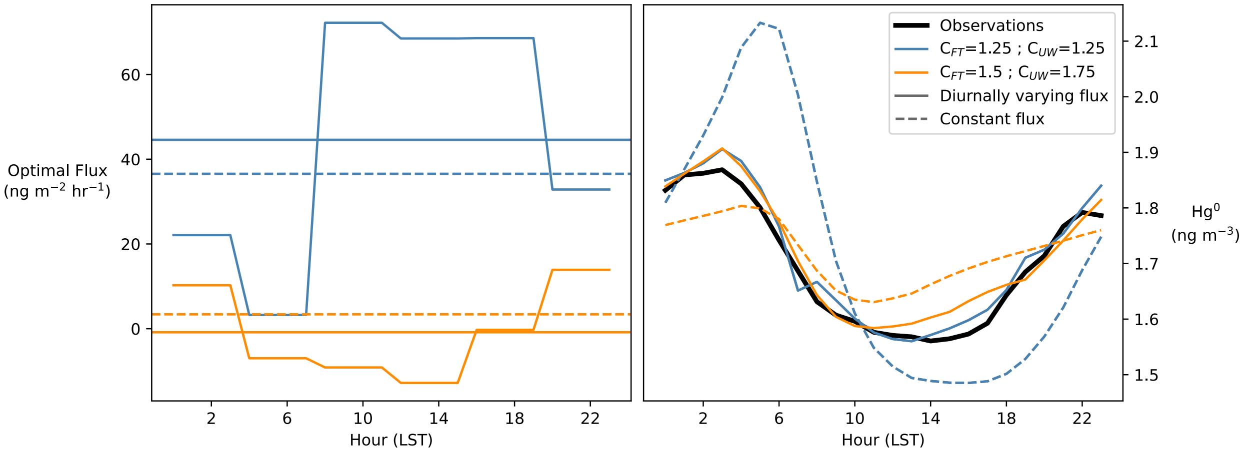

**Figure S8:** Comparison of the optimal constant flux and optimal diurnally varying flux for the two combinations of $C_{FT}$ and $C_{UW}$ shown in figure S6 (left) and the respective concentration variation (right). In both cases, the constant flux is similar in magnitude to the average of the temporally varying flux. Interestingly, for the case where $C_{FT}$ = 1.5 (orange), the optimal fluxes from both methods have different signs on average, as the variable optimal predicts positive nighttime fluxes and negative daytime fluxes.

## Section S4. List of GEOS-Chem simulations

**Table S1. List of GEOS-Chem simulations used**

| Simulation | Resolution | Domain | Emission notes |
|---|---|---|---|
| STND | 2°x2.5° | Global | GMA emissions |
| NEST | 0.5°x0.625° | 20°-70° N, 60°-100° W | GMA emissions |
| ANT3 | 0.5°x0.625° | 20°-70° N, 60°-100° W | GMA scaled by factor of 3 (domain: 40°-50° N, 70°-80° W) |
| ANT7 | 0.5°x0.625° | 20°-70° N, 60°-100° W | GMA scaled by factor of 7 (domain: 40°-50° N, 70°-80° W) |
| ANT10 | 0.5°x0.625° | 20°-70° N, 60°-100° W | GMA scaled by factor of 10 (domain: 40°-50° N, 70°-80° W) |
| ANT3-ENA | 0.5°x0.625° | 20°-70° N, 60°-100° W | GMA scaled by factor of 3 across entire nested domain that covers eastern North America (see Fig. 1) |
| ANT7-ENA | 0.5°x0.625° | 20°-70° N, 60°-100° W | GMA scaled by factor of 7 across entire nested domain that covers eastern North America (see Fig. 1) |
| ANT10-ENA | 0.5°x0.625° | 20°-70° N, 60°-100° W | GMA scaled by factor of 10 across entire nested domain that covers eastern North America (see Fig. 1) |
| CFTSCAL | 0.5°x0.625° | 20°-70° N, 60°-100° W | GMA emissions, $C_{FT}$ increased to approximately 1.4 ng $m^{-3}$ by applying spatially and temporally uniform emission source of 5 x $10^{-15}$ kg $m^{-2}$ $s^{-1}$ at 3500 m above ground level |
| CFTSCALMAX | 0.5°x0.625° | 20°-70° N, 60°-100° W | GMA emissions, $C_{FT}$ increased to approximately 1.8 ng $m^{-3}$ by applying spatially and temporally uniform emission source of 1 x $10^{-14}$ kg $m^{-2}$ $s^{-1}$ at 3500 m above ground level |

## Section S5. Relative contribution of chemical processing to $Hg^0$ fluxes within the PBL in GEOS-Chem

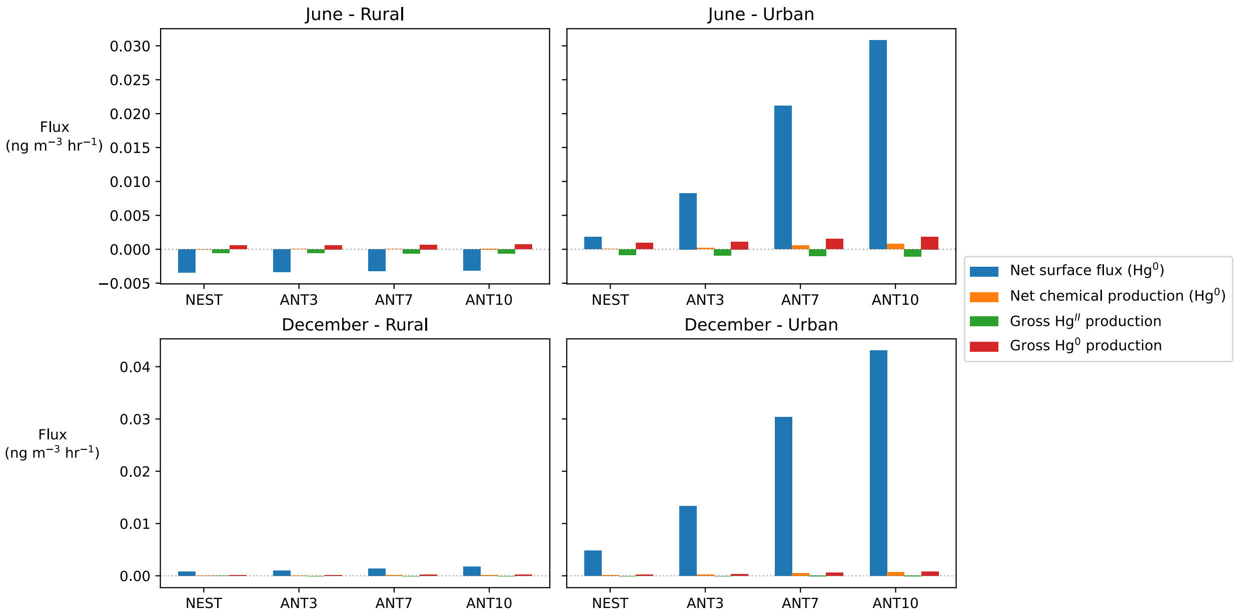

**Figure S9.** The relative magnitude of net surface fluxes and chemical fluxes within the planetary boundary layer in rural (left panels) and urban (right panels) regions, according to nested GEOS-Chem simulation in June (upper panels) and December (lower panels). Surface fluxes are normalized to represent their effect on average boundary layer concentrations by dividing by the average modeled PBLH for the respective month (see Fig S2). Regardless of the magnitude of anthropogenic emissions in this region, the magnitude of surface fluxes is 36-875 times larger than net chemical fluxes in the rural area and 21-30 times larger in the urban area.

## Section S6. Estimating $C_{FT}$ and $C_{UW}$ from GEOS-Chem simulations

We describe our approach for estimating $C_{FT}$ and $C_{UW}$ from GEOS-Chem output below. We first define broad upwind domains for the rural and urban regions (green and orange boxes, left panel of Figures S10-S15). The broad horizontal extents of the upwind domains are selected to dampen the occasional effect of temporally varying winds that may occasionally pass through areas that are strong sources or sinks. Additionally, their locations are selected to be representative of the respective region, with mixed urban and suburban areas in New Jersey and Pennsylvania representing the upwind region for urban sites and upstate New York representing upwind region for rural sites. $C_{UW}$ is calculated for each region as the average concentration within the upwind domains from the surface to the PBLH indicated by MERRA2 reanalysis. We define $C_{FT}$ as the average hourly concentration of the column extending from the PBLH to 700 hPa above the midpoint between the measurement sites for respective regions (right panels of Figures S10-S15). The vertical extent of the PBLH exhibits hourly variation, however there is little difference in the average PBLH and its extent between urban and rural sites, supporting our use of spatially aggregated profiles for box model simulations described in Section 2.2 of the main text.

The NEST, ANT7, and CFTSCAL simulations in June show the impact of enhancing concentrations on spatial and vertical distribution. In the NEST simulation, concentrations throughout the domain are low and are highest over the ocean (Figure S10). Concentrations at urban centers including NYC and Boston do not notably deviate from lower concentrations in rural areas of the Northeastern US. A similar vertical distribution of Hg is observed at both urban and rural regions, with lower concentrations near the surface and higher concentrations aloft. In the ANT7 simulation, concentrations at urban centers are noticeably higher than in rural areas of the northeastern US, illustrating expected differences between known sink and source regions (Figure S11). This is also observed in vertical cross-section plots, where concentrations in the urban upwind domain are notably higher near the surface, while there is little impact in the rural areas. Notably, concentrations aloft are far less sensitive to regional emission enhancements than surface concentrations. In the CFTSCAL simulation, we find that direct enhancements to $C_{FT}$ can effectively scale the surface features observed in the NEST simulation, with highest concentrations over the ocean and lower concentrations over land, consistent with the dominant influences of vegetative uptake fluxes and oceanic emissions in the model (Figure S12).

We also evaluate the vertical and horizontal distribution of Hg in the December sensitivity simulations (Figures S13-S15). Unlike June, there isn't a noticeable difference in $Hg^0$ concentrations between land and ocean in the NEST simulation (Figure S13). However, concentrations throughout the domain are notably higher in both horizontal and vertical dimensions in December, with highest concentrations in the southwestern portion of the domain (Figure S13). This is consistent with a lack of vegetative uptake in winter, resulting in a terrestrial shift from a summertime sink to wintertime source. We find that ANT7 results in large concentration enhancements near the surface that are more pronounced than in summer, which is likely driven by the combined influence of lower daytime PBLH and a lack of vegetative uptake to dampen this source (Figure S14). As in June, we find that the CFTSCAL simulation effectively enhances the existing spatial distribution of concentrations throughout the domain (Figure S15).

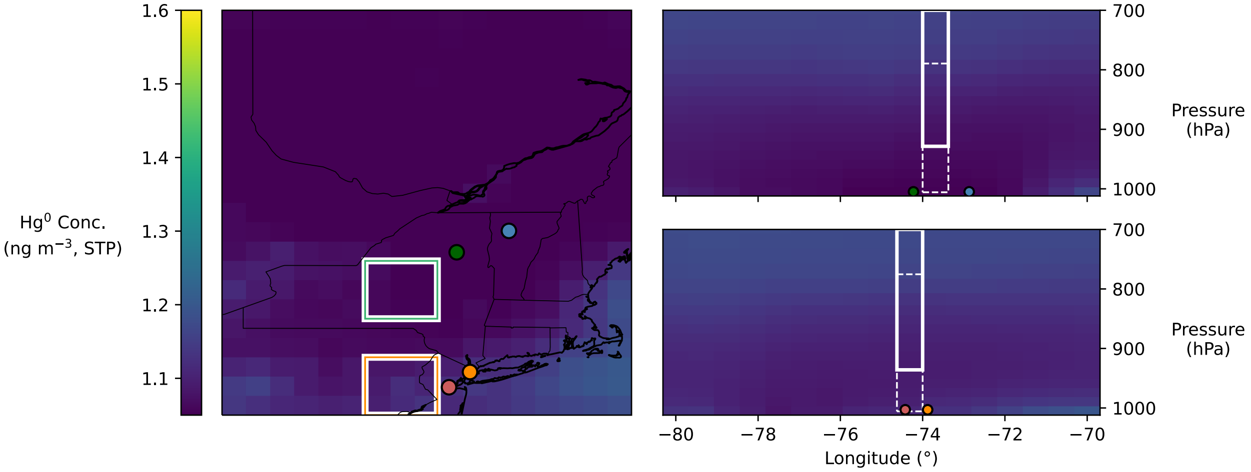

**Figure S10.** (left panel) Average surface concentration in June for the NEST simulation, where the green and orange boxes show the spatial region used to define CUW for rural and urban sites, respectively. The upper and lower right panels show a horizontal cross section of the rural and urban latitudes to illustrate the average vertical distribution. The solid white boxes show the average height of the grid cells used to calculate $C_{FT}$ in both regions, while the dashed lines show the range over which the lower bound of this region extends during the month.

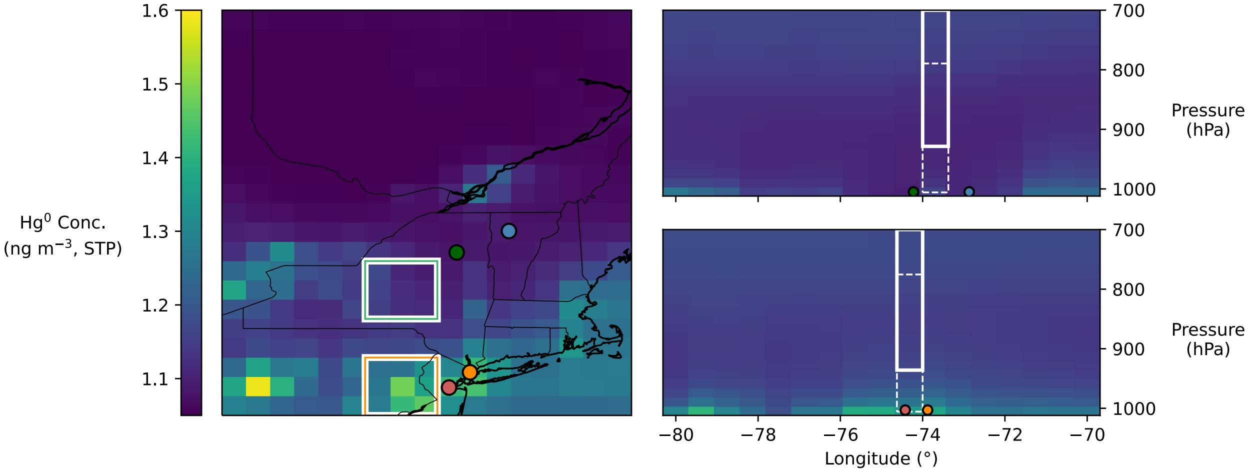

**Figure S11.** (left panel) Average surface concentration in June for ANT7 simulation, where the green and orange boxes show the spatial region used to define CUW for rural and urban sites, respectively. The upper and lower right panels show a horizontal cross section of the rural and urban latitudes to illustrate the average vertical distribution. The solid white boxes show the average height of the grid cells used to calculate $C_{FT}$ in both regions, while the dashed lines show the range over which the lower bound of this region extends during the month.

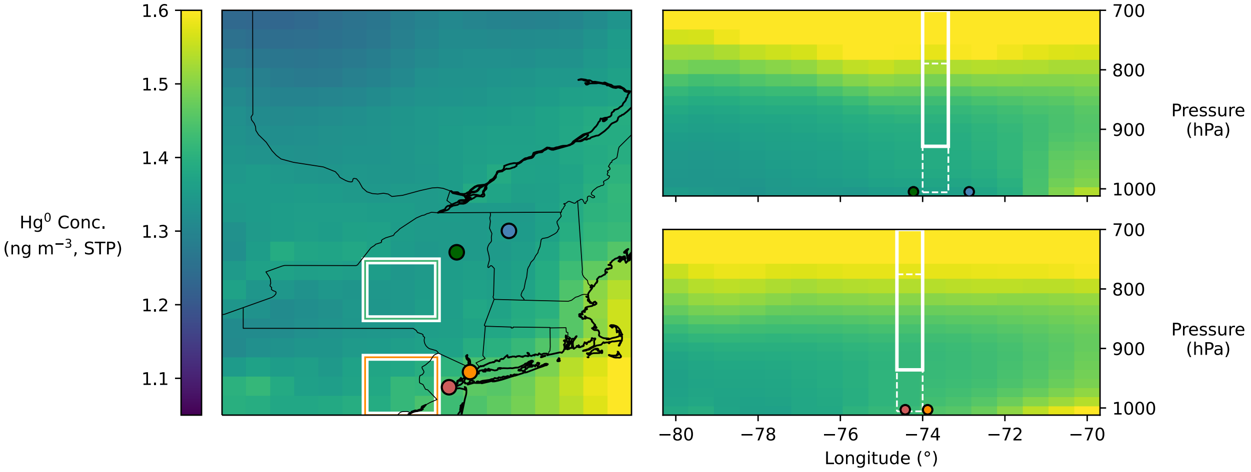

**Figure S12.** (left panel) Average surface concentration in June for the CFTSCAL simulation, where the green and orange boxes show the spatial region used to define CUW for rural and urban sites, respectively. The upper and lower right panels show a horizontal cross section of the rural and urban latitudes to illustrate the average vertical distribution. The solid white boxes show the average height of the grid cells used to calculate $C_{FT}$ in both regions, while the dashed lines show the range over which the lower bound of this region extends during the month.

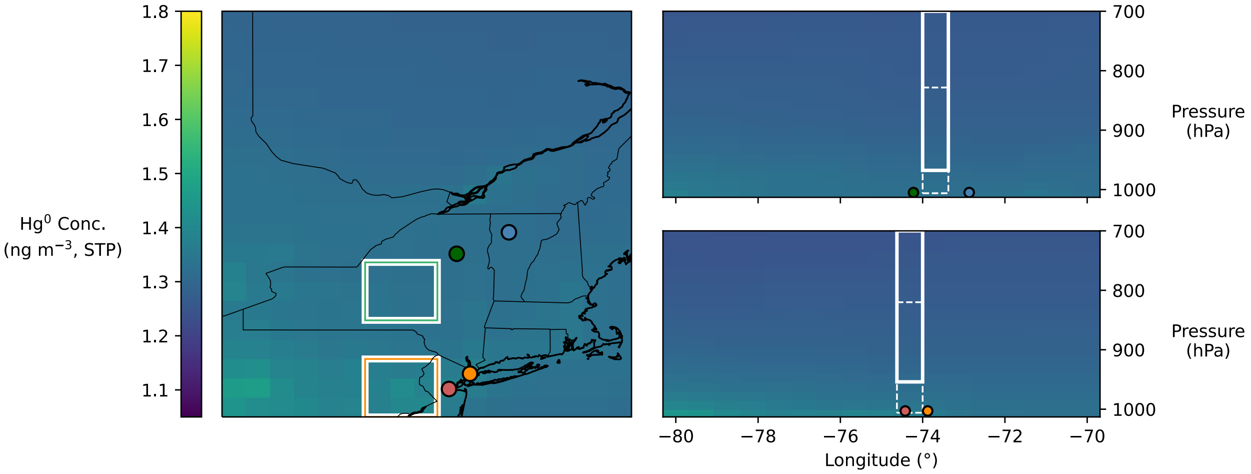

**Figure S13.** (left panel) Average surface concentration in December for the NEST simulation, where the green and orange boxes show the spatial region used to define CUW for rural and urban sites, respectively. The upper and lower right panels show a horizontal cross section of the rural and urban latitudes to illustrate the average vertical distribution. The solid white boxes show the average height of the grid cells used to calculate $C_{FT}$ in both regions, while the dashed lines show the range over which the lower bound of this region extends during the month.

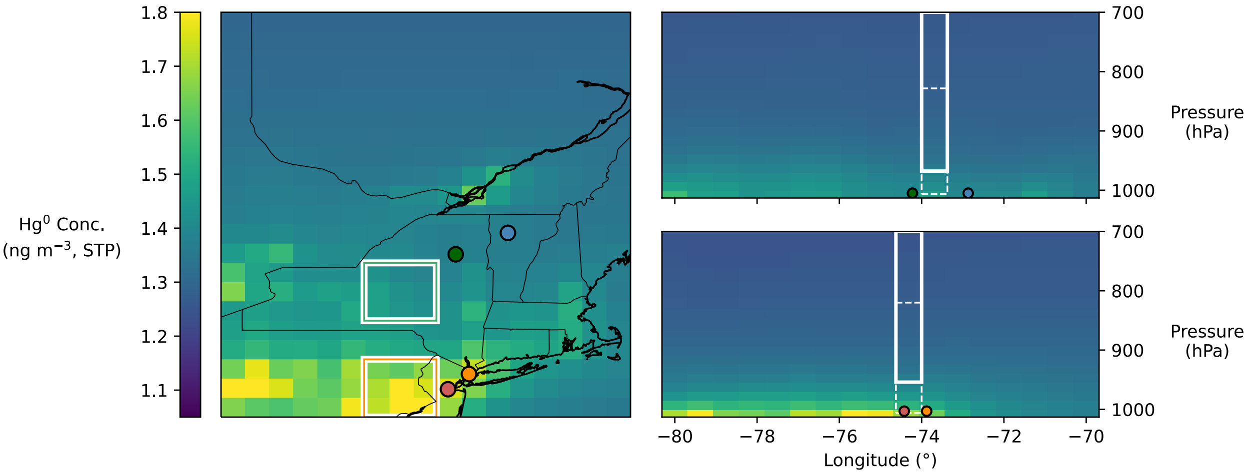

**Figure S14:** (left panel) Average surface concentration in December for the ANT7 simulation, where the green and orange boxes show the spatial region used to define CUW for rural and urban sites, respectively. The upper and lower right panels show a horizontal cross section of the rural and urban latitudes to illustrate the average vertical distribution. The solid white boxes show the average height of the grid cells used to calculate $C_{FT}$ in both regions, while the dashed lines show the range over which the lower bound of this region extends during the month.

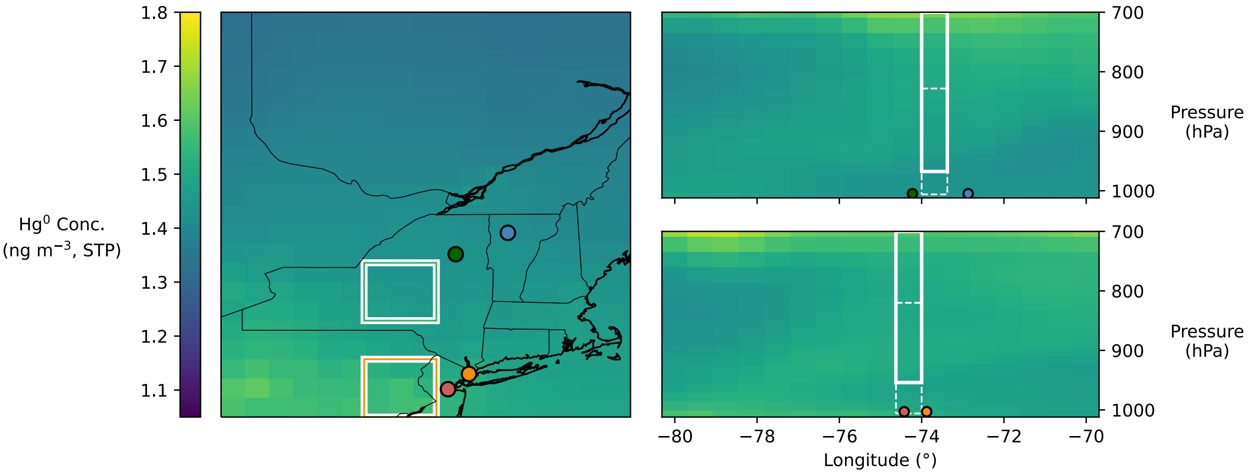

**Figure S15:** (left panel) Average surface concentration in December for the CFTSCAL simulation, where the green and orange boxes show the spatial region used to define CUW for rural and urban sites, respectively. The upper and lower right panels show a horizontal cross section of the rural and urban latitudes to illustrate the average vertical distribution. The solid white boxes show the average height of the grid cells used to calculate $C_{FT}$ in both regions, while the dashed lines show the range over which the lower bound of this region extends during the month.

## Section S7. Impacts of anthropogenic emission scaling across eastern North America

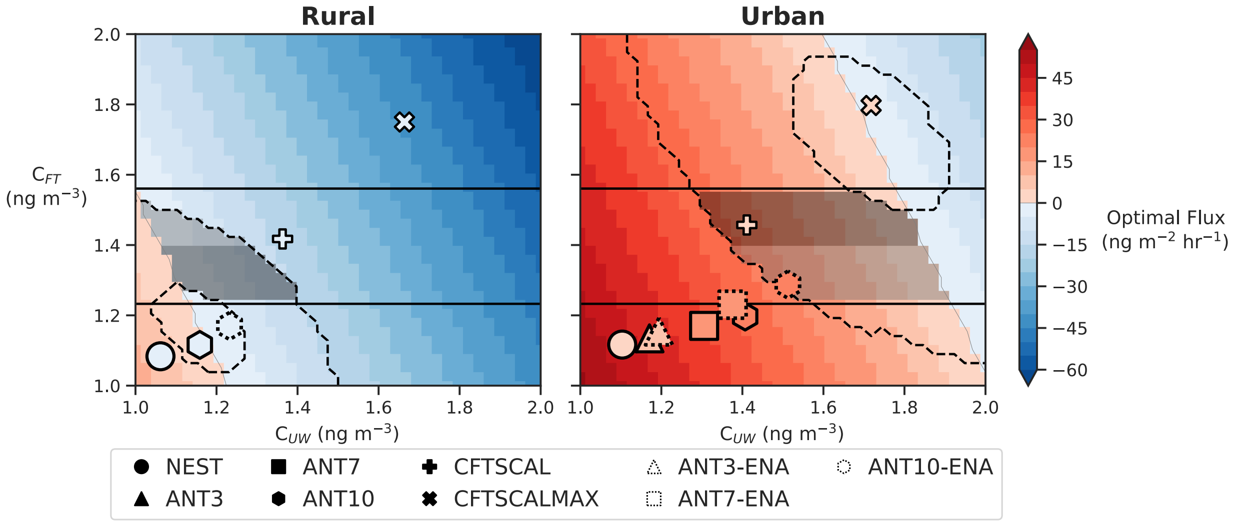

**Figure S16.** Same as figure 3 of main text, here including results from the ANT3-ENA, ANT7-ENA, and ANT10-ENA sensitivity simulations as dashed outline boxes. By expanding the region over which emissions are scaled, CFT and CUW also increase, with the latter having more sensitivity.

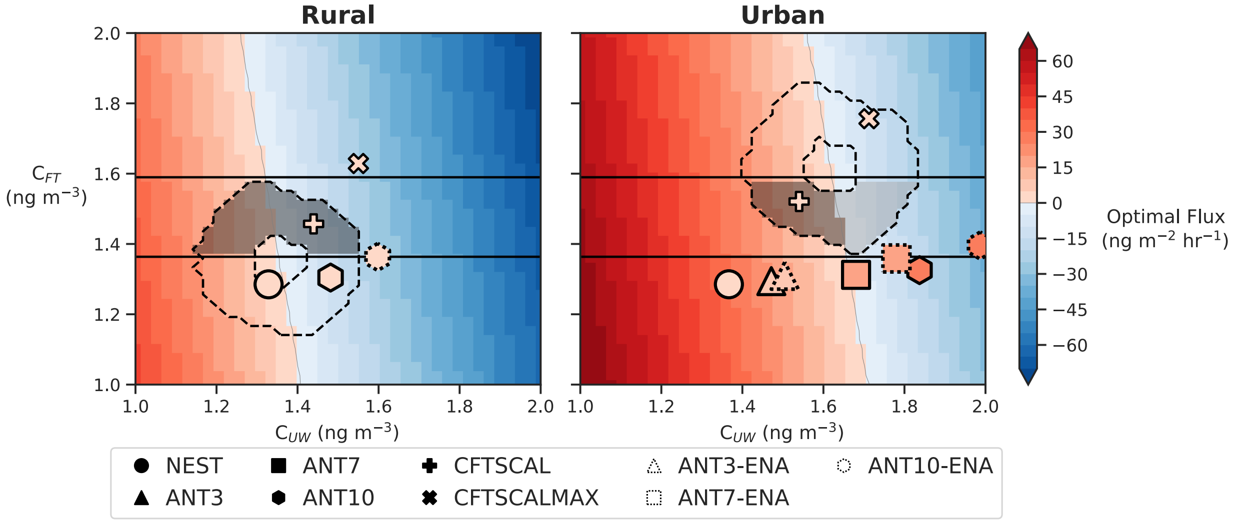

**Figure S17.** Same as figure 4 of main text, here including results from the ANT3-ENA, ANT7-ENA, and ANT10-ENA sensitivity simulations as dashed outline boxes. By expanding the region over which emissions are scaled, CFT and CUW also increase, with the latter having more sensitivity.

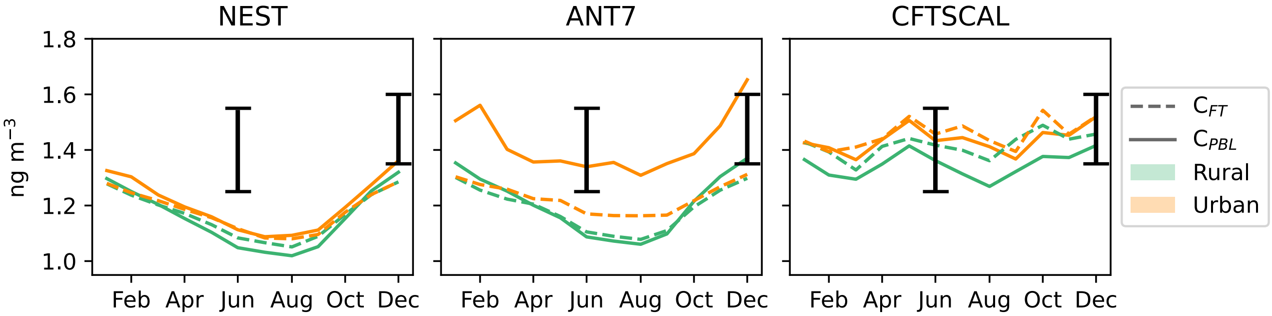

**Figure S18:** Seasonal variation of surface and free tropospheric concentrations ($C_{PBL}$ and $C_{FT}$, respectively) at rural (green) and urban (orange) regions in NEST, ANT7, and CFTSCAL simulations. Black bars represent observational constraints on $C_{FT}$ in June and December discussed in the main text. As previously discussed, NEST underestimates urban and rural $C_{PBL}$ in June and December. ANT7 improves the expected spatial gradient of $C_{PBL}$ but has limited impact on $C_{FT}$, which remains lower than observational constraints. Only the CFTSCAL simulation can satisfy observationally inferred constraints on $C_{FT}$, while also increasing the concentrations observed at the surface at these sites.